

Modelling the cyclic ratcheting of sands through memory-enhanced bounding surface plasticity

Liu, Haoyuan; Abell, J. A.; Diambra, A.; Pisano, Federico

DOI

[10.1680/jgeot.17.P.307](https://doi.org/10.1680/jgeot.17.P.307)

Publication date

2019

Document Version

Accepted author manuscript

Published in

Géotechnique

Citation (APA)

Liu, H., Abell, J. A., Diambra, A., & Pisano, F. (2019). Modelling the cyclic ratcheting of sands through memory-enhanced bounding surface plasticity. *Géotechnique*, 69(9), 783-800.
<https://doi.org/10.1680/jgeot.17.P.307>

Important note

To cite this publication, please use the final published version (if applicable).
Please check the document version above.

Copyright

Other than for strictly personal use, it is not permitted to download, forward or distribute the text or part of it, without the consent of the author(s) and/or copyright holder(s), unless the work is under an open content license such as Creative Commons.

Takedown policy

Please contact us and provide details if you believe this document breaches copyrights.
We will remove access to the work immediately and investigate your claim.

Modelling the cyclic ratcheting of sands through memory-enhanced bounding surface plasticity

H.Y. LIU*, J.A. ABELL†, A. DIAMBRA‡, F. PISANÒ*

The modelling and simulation of cyclic sand ratcheting is tackled via a plasticity model formulated within the well-known critical state, bounding surface SANISAND framework. For this purpose, a third locus – termed ‘memory surface’ – is cast into the constitutive formulation, so as to phenomenologically capture micro-mechanical, fabric-related processes directly relevant to the cyclic response. The predictive capability of the model under numerous loading cycles (‘high-cyclic’ loading) is explored with focus on drained loading conditions, and validated against experimental test results from the literature – including triaxial, simple shear and oedometer cyclic loading. The model proves capable of reproducing the transition from ratcheting to shakedown response, in combination with a single set of soil parameters for different initial, boundary and loading conditions. This work contributes to the analysis of soil-structure interaction under high-cyclic loading events, such as those induced by environmental and/or traffic loads.

KEYWORDS: sands, stiffness, constitutive relations, plasticity, numerical modelling, offshore engineering

INTRODUCTION

Predicting the cyclic response of sands is relevant to numerous geotechnical applications, for instance in the fields of earthquake, offshore and railway engineering. Such a response emerges from complex micro-mechanical processes that give rise to a highly non-linear hydro-mechanical behaviour at the macro-scale, featuring irreversible deformation, hysteresis, pore pressure build-up, etc. (di Prisco & Muir Wood, 2012). The engineering analysis of these phenomena proves even more challenging for long-lasting cyclic loading events (‘high-cyclic’ loading), such as those experienced by soils and foundations under operating offshore structures (e.g. offshore drilling rigs, pipelines, wind turbines) (Andersen, 2009, 2015; Randolph & Gourvenec, 2011). A typical example is given at present by monopile foundations for offshore wind turbines, whose design must assure full functionality of the structure during its whole operational life – 10^8 - 10^9 loading cycles with alternating sequences of small-amplitude vibrations and severe storm loading (LeBlanc *et al.*, 2010; Abadie, 2015).

Despite the current ferment around offshore wind geotechnics (Pisanò & Gavin, 2017), frustrating uncertainties still affect the engineering analyses performed to assess the capacity, serviceability and fatigue resistance of wind turbine foundations. In this context, a major role is played by the phenomenon of ‘sand ratcheting’: this term denotes the gradual accumulation of plastic strains under many loading cycles, as opposed to the occurrence of ‘shakedown’ (long-term response with no plastic strain accumulation) (Houlsby *et al.*, 2017). While micromechanical studies aim to describe the occurrence and modes of sand ratcheting at the granular level (Alonso-Marroquin & Herrmann, 2004;

McNamara *et al.*, 2008; O’Sullivan & Cui, 2009; Calvetti & di Prisco, 2010), usable engineering methods are currently being devised for predictions at the soil-foundation-structure scale. Serious challenges arise in this area for at least two reasons: (i) the time-domain, step-by-step analysis of high-cyclic soil-structure interaction (‘implicit analysis’, in the terminology of Niemunis *et al.* (2005)) is computationally prohibitive and challenging accuracy-wise; (ii) even with viable implicit computations (e.g. through intensive parallel computing), the literature still lacks constitutive models reproducing cyclic sand ratcheting with satisfactory accuracy.

To mitigate the above difficulties, alternative ‘explicit’ methods have been proposed, including some recent applications to offshore wind turbine foundations (Suiker & de Borst, 2003; Niemunis *et al.*, 2005; Achmus *et al.*, 2009; Wichtmann *et al.*, 2010; Andresen *et al.*, 2010; Pasten *et al.*, 2013; Jostad *et al.*, 2014, 2015; Triantafyllidis *et al.*, 2016; Chong, 2017). In this framework, sand cyclic straining is directly linked to the number of loading cycles N – hence the term ‘explicit’. Accordingly, the relationship between accumulated strains and N emerges from empirical relationships accounting for micro-structural/mechanical properties (void ratio, grain size distribution, shear strength, etc.) and loading parameters (stress or strain amplitude, confining pressure, deviatoric obliquity, etc.), to be calibrated based on rare high-cyclic laboratory tests – see e.g. Lekarp *et al.* (2000); Suiker *et al.* (2005); Wichtmann (2005); Wichtmann *et al.* (2005); Wichtmann & Triantafyllidis (2015); Wichtmann *et al.* (2015); Escribano *et al.* (2018). Most often, explicit high-cyclic methods are used in combination with implicit calculation stages: the latter provide the space distribution of cyclic stress/strain increments via the time-domain simulation of one/two loading cycles; the former feed such information to empirical strain accumulation models and derive global high-cyclic deformations at increasing N (Niemunis *et al.*, 2005; Andresen *et al.*, 2010; Pasten *et al.*, 2013). Although significantly faster than implicit time marching, stability and accuracy issues may be experienced in explicit N -stepping (Pasten *et al.*, 2013).

The present work tackles the modelling of sand ratcheting within the phenomenological framework of bounding surface

Manuscript received . . .

*Geo-Engineering Section, Faculty of Civil Engineering and Geoscience, Delft University of Technology, Stevinweg 1, 2628 CN Delft (The Netherlands)

† Facultad de Ingeniería y Ciencias Aplicadas, Universidad de los Andes, Mons. Álvaro del Portillo 12.455, 762000111, Las Condes, Santiago (Chile)

‡ Department of Civil Engineering, Faculty of Engineering, University of Bristol, Queen’s Building, University Walk, Clifton BS8 1TR, Bristol (United Kingdom).

plasticity. For this purpose, the critical state SANISAND04 model by Dafalias & Manzari (2004) is enriched with a third locus – termed ‘memory surface’ – to reproduce fabric effects relevant to cyclic ratcheting. The suitability of the memory surface approach has been recently shown by Corti (2016) and Corti *et al.* (2016) in combination with the bounding surface model by Gajo & Muir Wood (1999b,a). The resulting model has been successfully applied to the cyclic analysis of certain offshore soil-structure interaction problems, involving e.g. mudmat foundations (Corti *et al.*, 2017) and plate anchors (Chow *et al.*, 2015). In this work, the SANISAND conceptual platform has been preferred also in light of the several open-source implementations already available (Mazzoni *et al.*, 2007; Gudehus *et al.*, 2008; Ghofrani & Arduino, 2017), which will enable to move faster towards the analysis of relevant boundary value problems.

With main focus on drained loading conditions, the model described in the following improves the achievements of Corti *et al.* in several respects: (i) general multiaxial formulation, with pressure-sensitive hardening rules suitable to accommodate the different backbone model (SANISAND04) under monotonic and cyclic loading; (ii) improved analytical “workability” achieved through a formulation based on the “true” stress tensor, and the use of a memory locus with circular deviatoric section; (iii) modified plastic flow rule to refine the simulation of volume changes under cyclic loading conditions. Importantly, the ratcheting performance of the model has been tested up to 10^4 loading cycles, and validated against a wider set of literature results, including triaxial (both standard and non-standard), simple shear and oedometer high-cyclic tests.

The ultimate goal of this paper is to help bridge implicit and explicit approaches through the proposed plasticity model. Its ‘implicit’ use will enable more accurate time-domain simulations of cyclic/dynamic soil-structure interaction under relatively short-lasting loading (e.g. storms, earthquakes, etc.) (Corciulo *et al.*, 2017). As more experimental data become available and further calibration exercises carried out, it will also contribute to explicit high-cyclic procedures by supporting the prediction of strain accumulation trends with lower demand of laboratory test results.

TOWARDS A SANISAND MODEL WITH RATCHETING CONTROL

While massive efforts have been devoted to modelling the undrained cyclic behaviour of sands, the cyclic performance under drained loading conditions has received far less attention. A few works tackled this issue by enhancing the bounding surface framework with fabric-related modelling concepts, such as Khalili *et al.* (2005); Kan *et al.* (2013); Gao & Zhao (2015); outside traditional bounding surface plasticity, the contributions by Wan & Guo (2001); Di Benedetto *et al.* (2014); Liu *et al.* (2014); Tasiopoulou & Gerolymos (2016) are also worth citing. However, none of the mentioned works focused explicitly on drained strain accumulation under a large number of loading cycles.

The cyclic sand model proposed in this study builds upon two main pillars, namely the SANISAND04 model by Dafalias & Manzari (2004) and the addition of a memory locus accounting for fabric effects during cyclic loading (Corti, 2016; Corti *et al.*, 2016). Since its first introduction in 1997 (Manzari & Dafalias, 1997), the family of SANISAND models has expanded with new members improving certain limitations of the original formulation, regarding e.g. dilatancy and fabric effects,

hysteretic small-strain behaviour, response to radial stress paths, incremental non-linearity (Papadimitriou *et al.*, 2001; Papadimitriou & Bouckovalas, 2002; Dafalias & Manzari, 2004; Taiebat & Dafalias, 2008; Loukidis & Salgado, 2009; Pisanò & Jeremić, 2014; Dafalias & Taiebat, 2016). In particular, the SANISAND04 formulation includes a fabric-related tensor improving the phenomenological simulation of post-dilation fabric changes upon load reversals, with beneficial impact on the prediction of pore pressure build-up during undrained cyclic loading.

Unfortunately, the set of modelling ingredients as conjugated in SANISAND04 cannot quantitatively reproduce high-cyclic ratcheting, nor its dependence on relevant loading parameters (especially stress obliquity, symmetry and amplitude of the loading programme). In SANISAND04, (i) the use of the (phenomenological) fabric tensor \mathbf{z} is only suitable to capture the effects of initial inherent anisotropy, as explained in detail by Li & Dafalias (2011); (ii) fabric evolution is solely activated for denser-than-critical conditions, after the stress path crosses the phase transformation line. This latter strategy has proven not sufficient to capture fabric effects occurring during (drained) cyclic loading, for instance related to the evolving distributions of voids and particle contacts (Oda *et al.*, 1985; O’Sullivan *et al.*, 2008; Zhao & Guo, 2013). A significant impact of these facts on numerical simulations is that the SANISAND04 model produces only slight soil stiffening under drained (high-)cyclic shear loading, resulting in exaggerated strain accumulation. While acknowledging the benefits of improved fabric tensor formulations (Papadimitriou & Bouckovalas, 2002), a different path based on the memory surface concept will be followed in the remainder of this work.

The plasticity modelling of ratcheting phenomena has received a few valuable contributions (di Prisco & Mortara, 2013), originally regarding metals and alloys. These contributions have been reviewed by Houlsby *et al.* (2017), and generalised into a hyper-plastic multi-surface framework for the macro-element analysis of offshore monopiles.

The present paper proposes an alternative approach based on bounding surface plasticity and the use of an additional memory surface to keep track of fabric changes relevant to the ratcheting response. The concept of memory surface (or history surface) was first proposed by Stallebrass & Taylor (1997) for overconsolidated clays, then applied to sands within different modelling frameworks by Jafarzadeh *et al.* (2008); Maleki *et al.* (2009); Di Benedetto *et al.* (2014). Herein, the latest version by Corti *et al.* (2016) and Corti (2016) is adopted and enhanced within the SANISAND family. Accordingly, the regions of the stress-space that have already experienced cyclic loading are represented by an evolving memory locus, within which cyclic strain accumulation occurs at a lower rate than under virgin loading conditions.

MODEL FORMULATION

This section presents the main analytical features of the proposed model, with focus on embedding the memory surface concept into the SANISAND04 backbone formulation. Similarly to SANISAND04, the new model is based on a bounding surface, kinematic hardening formulation to capture cyclic, rate-independent behaviour. The model links to the well-established Critical State theory through the notion of ‘state parameter’ (Been & Jefferies, 1985), which enables to span the behaviour of a given sand over the loose-to-dense range with a single set of parameters. Overall, the new model uses three relevant loci – yield,

bounding and memory surface (Figure 1). All constitutive equations are presented by first summarising the features inherited from Dafalias & Manzari (2004), then focusing on the latest memory surface developments.

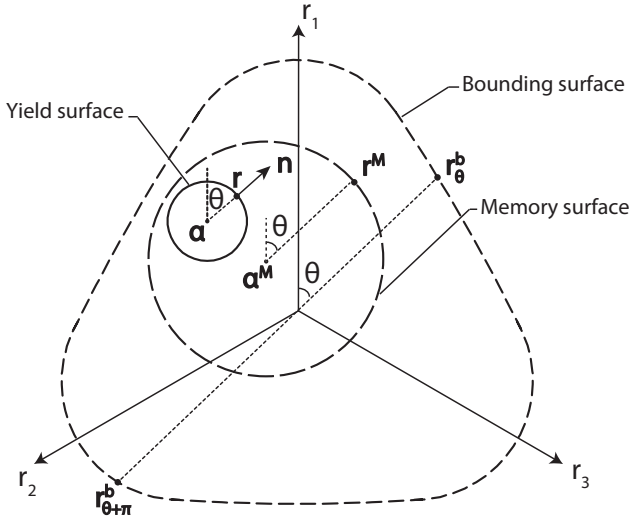


Fig. 1. Relevant loci/tensors in the normalised π plane.

Notation Tensor quantities are denoted by bold-face characters in a direct notation. The symbols $:$, tr and $\langle \rangle$ stand for tensor inner product, trace operator and Macauley brackets, respectively.

$\boldsymbol{\sigma}$ and $\boldsymbol{\varepsilon}$ denote effective stress* and strain tensor. Usual decompositions into deviatoric and isotropic components are used throughout, namely $\boldsymbol{\sigma} = \boldsymbol{s} + p\mathbf{I}$ (\boldsymbol{s} - deviatoric stress tensor, $p = (\text{tr}\boldsymbol{\sigma})/3$ - isotropic mean stress) and $\boldsymbol{\varepsilon} = \boldsymbol{e} + (\varepsilon_{vol}/3)\mathbf{I}$ (\boldsymbol{e} - deviatoric strain tensor, $\varepsilon_{vol} = \text{tr}\boldsymbol{\varepsilon}$ - volumetric strain). \mathbf{I} is the second-order identity tensor, the deviatoric stress ratio $\boldsymbol{r} = \boldsymbol{s}/p$ is also widely employed in the formulation. The superscripts e and p are used with the meaning of ‘elastic’ and ‘plastic’.

Model features from SANISAND04

For the sake of brevity, a multi-axial formulation is directly provided, while conceptual discussions in a simpler triaxial environment may be found in the aforementioned publications. For the same reason, model details shared with SANISAND04 are only briefly recalled, whereas Table 1 provides a synopsis of all equations and material parameters (Dafalias & Manzari, 2004).

Similarly to most SANISAND formulations, the proposed model relies on the assumption that plastic stains only occur upon variations in stress ratio \boldsymbol{r} , so that all plastic loci and hardening mechanisms can be effectively described in the normalised π plane (Figure 1). Importantly, the overall formulation remains based on ‘true’ stress ratio variables, while Gajo & Muir Wood (1999a,b); Corti *et al.* (2016) used stress normalised with respect to the current state parameter.

Elastic relationship Sand behaviour is assumed to be (hypo)elastic inside the yield locus, with constant Poisson ratio ν and pressure-dependent shear modulus defined as

per Richart *et al.* (1970); Li & Dafalias (2000):

$$G = G_0 p_{atm} [(2.97 - e)^2 / (1 + e)] \sqrt{p/p_{atm}} \quad (1)$$

in which p_{atm} is the reference atmospheric pressure, G_0 a dimensionless shear stiffness parameter, and e the current void ratio.

Yield locus An open conical yield locus $f = 0$ is used, whose axis rotation and (constant) small opening are governed by the evolution of the back-stress ratio $\boldsymbol{\alpha}$ and the parameter m :

$$f = \sqrt{(\boldsymbol{s} - p\boldsymbol{\alpha}) : (\boldsymbol{s} - p\boldsymbol{\alpha})} - \sqrt{2/3}mp = 0 \quad (2)$$

Critical state locus A unique critical state locus is assumed and defined in the multidimensional $e - \boldsymbol{\sigma}$ space. Its projection on the $e - p$ plane, i.e. the critical state line, reads as (the subscript c stands for ‘critical’):

$$e_c = e_0 - \lambda_c (p_c/p_{atm})^\xi \quad (3)$$

and requires the identification of three material parameters - e_0 , λ_c and ξ (Li & Wang, 1998). The aforementioned state parameter $\Psi(e, p) = e - e_c$ quantifies the distance between current and critical void ratios (Been & Jefferies, 1985; Muir Wood & Belkheir, 1994), which is key to modelling sand behaviour at varying relative density.

The projection of the critical state locus on the normalised π plane can be conveniently expressed as a deviatoric tensor \boldsymbol{r}_θ^c :

$$\boldsymbol{r}_\theta^c = \sqrt{2/3}g(\theta)M\boldsymbol{n} \quad (4)$$

providing the critical state stress ratio associated with the current stress ratio \boldsymbol{r} through the unit tensor, normal to the yield locus (Figure 1):

$$\boldsymbol{n} = (\boldsymbol{r} - \boldsymbol{\alpha}) / \sqrt{2/3}m \quad (5)$$

The function g describes the Argyris-type shape of the critical locus depending on the ‘relative’ Lode angle θ^\dagger (see Table 1 and Dafalias & Manzari (2004)). The parameter M appears in its traditional meaning of critical stress ratio under triaxial compression (directly related to the constant-volume friction angle).

It should also be recalled that the assumption of unique critical state locus is still a matter of scientific debate, and certainly not the only option available - nonetheless, a several theoretical studies may be cited in its support (Li & Dafalias, 2011; Zhao & Guo, 2013; Gao & Zhao, 2015). An evolving version of the locus (Equation(3)) could be adopted in the future upon conclusive consensus on the subject - for instance, according to the path followed by Papadimitriou *et al.* (2005).

Plastic flow rule Plastic strain increments - deviatoric and volumetric - are obtained as:

$$d\boldsymbol{\varepsilon}^p = \langle L \rangle \boldsymbol{R}' \quad d\varepsilon_{vol}^p = \langle L \rangle D \quad (6)$$

where \boldsymbol{R}' and D are the tensor of deviatoric plastic flow direction (Dafalias & Manzari, 2004) and the dilatancy coefficient, respectively. The plastic multiplier L (or loading

*As this work focuses on drained tests/simulations, the notation $\boldsymbol{\sigma}$ (instead of usual $\boldsymbol{\sigma}'$) is used for the effective stress tensor with no ambiguity.

$\dagger \cos 3\theta = \sqrt{6}tr\boldsymbol{n}^3$ (Manzari & Dafalias, 1997)

index) results from the enforcement of plastic consistency and can be expressed in the following form:

$$L = \frac{1}{K_p} \frac{\partial f}{\partial \boldsymbol{\sigma}} : d\boldsymbol{\sigma} \quad (7)$$

with K_p commonly referred to as plastic modulus.

Kinematic hardening and bounding surface The back-stress ratio $\boldsymbol{\alpha}$ (axis of the yield locus) is assumed to evolve according to the following hardening law:

$$d\boldsymbol{\alpha} = \frac{2}{3} \langle L \rangle h (\mathbf{r}_\theta^b - \mathbf{r}) \Rightarrow K_p = \frac{2}{3} ph (\mathbf{r}_\theta^b - \mathbf{r}) : \mathbf{n} \quad (8)$$

which in turn implies the expression of K_p reported beside (Dafalias & Manzari, 2004). According to Equation (8), the centre of the yield locus translates in the π plane along the $\mathbf{r}_\theta^b - \mathbf{r}$ direction, with magnitude governed by the hardening factor h . \mathbf{r}_θ^b represents the projection of the current stress ratio onto the so-called bounding surface:

$$\mathbf{r}_\theta^b = \sqrt{2/3} g(\theta) M \exp(-n^b \Psi) \mathbf{n} \quad (9)$$

The size of the bounding surface is modulated by the state parameter Ψ and the corresponding material constant n^b . At critical state $\Psi = 0$ and the bounding surface coincides with the critical locus. It is worth noting that, for better compatibility with memory surface developments, the present formulation reappraises projection rules based on the stress ratio \mathbf{r} rather than the back-stress ratio $\boldsymbol{\alpha}$ – compare e.g. Dafalias (1986) to Manzari & Dafalias (1997).

Additional memory surface for ratcheting control

Novel developments related to the memory surface concept are detailed in this subsection, with direct impact on the factors h and D in Equations (8) and (6).

Meaning and definition

Figure 1 illustrates in the normalised π plane the three main loci involved in the model formulation:

- *yield surface*, distinguishes stress states associated with either negligible or significant plastic straining;
- *memory surface*, distinguishes stress states associated with either vanishing or severe changes in granular fabric;
- *bounding surface*, separates admissible/pre-failure and ultimate stress states;

Although the above transitions may not be as sharp in nature, the above idealisation provides conceptual input to phenomenological constitutive modelling.

The memory locus is deployed to track the global (re)orientation of particle contacts, and in turn the degree of loading-induced anisotropy. Accordingly, it will be possible to describe weak fabric changes induced by moderate high-cyclic loads, possibly ‘overwritten’ by more severe loading afterwards – henceforth termed ‘virgin loading’ (Nemat-Nasser, 2000; Jafarzadeh *et al.*, 2008).

From an analytical standpoint, the memory locus $f^M = 0$ is represented by an additional conical surface:

$$f^M = \sqrt{(\mathbf{s} - p\boldsymbol{\alpha}^M) : (\mathbf{s} - p\boldsymbol{\alpha}^M)} - \sqrt{2/3} m^M p = 0 \quad (10)$$

endowed with its own (memory) back-stress ratio and opening variable $\boldsymbol{\alpha}^M$ and m^M . As shown in the following,

the choice of a conical memory locus with circular deviatoric section results in simpler projection rules and evolution laws (no lengthy algebra from the differentiation of the third stress invariant). Nevertheless, keeping the typical Argyris-shape for the outer bounding surface (Equation (9)) preserves a dependence of both stiffness and strength on the Lode angle θ .

It is postulated that, during plastic straining, (i) the stress point on the yield surface can never lie outside the memory surface, (ii) the memory surface can only be larger than the elastic domain, or at most coincident. These requisites are compatible with the following reformulation of the hardening coefficient h in K_p :

$$h = \frac{b_0}{(\mathbf{r} - \mathbf{r}_{in}) : \mathbf{n}} \exp \left[\mu_0 \left(\frac{p}{p_{atm}} \right)^{n=0.5} \left(\frac{b^M}{b_{ref}} \right)^{w=2} \right] \quad (11)$$

in which

$$\begin{aligned} b^M &= (\mathbf{r}^M - \mathbf{r}) : \mathbf{n} \\ b_{ref} &= (\mathbf{r}_\theta^b - \mathbf{r}_{\theta+\pi}^b) : \mathbf{n} \end{aligned} \quad (12)$$

and $\mathbf{r}_{\theta+\pi}^b$ is the opposite projection onto the bounding surface, along the direction $-\mathbf{n}$ with relative Lode angle $\theta + \pi$ (Equation (9), Figure 1 – therefore, $b_{ref} > 0$ always). The SANISAND04 definition of the hardening factor b_0 is recalled in Table 1. The above definitions include the image stress point \mathbf{r}^M on the memory surface, pointed by the unit tensor \mathbf{n} defined above (Equation (5)):

$$\mathbf{r}^M = \boldsymbol{\alpha}^M + \sqrt{2/3} m^M \mathbf{n} \quad (13)$$

The left factor in Equation (11) coincides with the h coefficient in Dafalias & Manzari (2004) (with b_0 model parameter and \mathbf{r}_{in} load-reversal tensor[‡]), whilst the right factor introduces the memory surface concept into SANISAND04 with the additional material parameter μ_0 (Corti *et al.*, 2016, 2017). In essence, h receives additional influence from the yield-to-memory surface distance b^M : as a consequence, higher K_p and soil stiffness result at increasing distance b^M (see evolution laws later on), but a virgin SANISAND04 response is recovered when the yield and the memory loci are tangent at the current stress point $\boldsymbol{\sigma} \equiv \boldsymbol{\sigma}^M$ ($\rightarrow b^M = 0$).

The two material parameters, n and w , have been pre-set in Equation (11) to mitigate calibration efforts. In particular, extensive comparisons to experimental data (see next sections) confirmed the need for a pressure-dependent memory surface term (Corti *et al.*, 2017), along with a quadratic dependence on the distance b^M . Additional experimental evidence may support in the future more flexibility about n and w , as well as other fundamental dependences (for instance on the void ratio e).

The following subsections introduce the evolution laws for the size and position of the memory surface, as well its effect on sand dilatancy.

Memory surface size

The expansion of the memory surface (isotropic hardening) aims to capture phenomenologically the experimental link between gradual change in fabric and sand stiffening.[§] This evidence is translated into an increasing size m^M of the

[‡] \mathbf{r}_{in} is the value of \mathbf{r} at the onset of load reversal. It is updated to current \mathbf{r} each time the condition $(\mathbf{r} - \mathbf{r}_{in}) : \mathbf{n} < 0$ is fulfilled.

[§]The effects of a varying void ratio are already accounted for as inheritance from SANISAND04.

Table 1. Model synopsis: constitutive equations and material parameters.

	Constitutive equations	Material parameters
Elastic moduli	$G = G_0 p_{atm} [(2.97 - e)^2 / (1 + e)] (p / p_{atm})^{1/2}$ $K = 2(1 + \nu)G / [3(1 - 2\nu)]$	G_0 dimensionless shear modulus ν Poisson's ratio
Critical state line	$e_c = e_0 - \lambda_c (p_c / p_{atm})^\xi$	e_0 reference critical void ratio λ_c, ξ critical state line shape parameters
Yield function	$f = \sqrt{(\mathbf{s} - p\boldsymbol{\alpha}) : (\mathbf{s} - p\boldsymbol{\alpha})} - \sqrt{2/3}pm$	m yield locus opening parameter
Memory function	$f^M = \sqrt{(\mathbf{s} - p\boldsymbol{\alpha}^M) : (\mathbf{s} - p\boldsymbol{\alpha}^M)} - \sqrt{2/3}pm^M$	
Deviatoric plastic flow	$d\mathbf{e}^p = \langle L \rangle \mathbf{R}'$ $\mathbf{R}' = B\mathbf{n} - C [\mathbf{n}^2 - (1/3)\mathbf{I}]$ $\mathbf{n} = (\mathbf{r} - \boldsymbol{\alpha}) / \sqrt{2/3}m$ $B = 1 + 3(1 - c) / (2c)g(\theta) \cos 3\theta$ $C = 3\sqrt{3}/2(1 - c)g(\theta)/c$ $g(\theta) = 2c / [(1 + c) - (1 - c) \cos 3\theta]$	
Volumetric plastic flow	$d\varepsilon_{vol}^p = \langle L \rangle D$ $D = \left[A_0 \exp \left(\beta \langle \dot{b}_d^M \rangle / b_{ref} \right) \right] (\mathbf{r}_\theta^d - \mathbf{r}) : \mathbf{n}$ $\mathbf{r}_\theta^d = \sqrt{2/3}g(\theta)M \exp(n^d \Psi) \mathbf{n}$ $\dot{b}_d^M = (\dot{\mathbf{r}}_\theta^d - \dot{\mathbf{r}}^M) : \mathbf{n}$ $b_{ref} = (\mathbf{r}_\theta^b - \mathbf{r}_{\theta+\pi}^b) : \mathbf{n}$ $\mathbf{r}_{\theta+\pi}^b = \sqrt{2/3}g(\theta + \pi)M \exp(-n^b \Psi)(-\mathbf{n})$	A_0 'intrinsic' dilatancy parameter β dilatancy memory parameter n^d void ratio dependence parameter
Yield surface evolution	$d\boldsymbol{\alpha} = (2/3) \langle L \rangle h(\mathbf{r}_\theta^b - \mathbf{r})$ $\mathbf{r}_\theta^b = \sqrt{2/3}g(\theta)M \exp(-n^b \Psi) \mathbf{n}$ $h = \frac{b_0}{(\mathbf{r} - \mathbf{r}_{in}) : \mathbf{n}} \exp \left[\mu_0 \left(\frac{p}{p_{atm}} \right)^{0.5} \left(\frac{b^M}{b_{ref}} \right)^2 \right]$ $b_0 = G_0 h_0 (1 - c_h e) / \sqrt{(p/p_{atm})}$ $b^M = (\mathbf{r}^M - \mathbf{r}) : \mathbf{n}$	M critical stress ratio (triaxial compression) n^b void ratio dependence parameter c compression-to-extension strength ratio μ_0 ratcheting parameter h_0, c_h hardening parameters
Memory surface evolution	$dm^M = \sqrt{3/2} d\boldsymbol{\alpha}^M : \mathbf{n} - (m^M / \zeta) f_{shr} \langle -d\varepsilon_{vol}^p \rangle$ $d\boldsymbol{\alpha}^M = (2/3) \langle L^M \rangle h^M (\mathbf{r}_\theta^b - \mathbf{r}^M)$ $h^M = \frac{1}{2} \left[\frac{b_0}{(\mathbf{r}^M - \mathbf{r}_{in}) : \mathbf{n}} + \sqrt{\frac{3}{2}} \frac{m^M f_{shr} \langle -D \rangle}{\zeta (\mathbf{r}_\theta^b - \mathbf{r}^M) : \mathbf{n}} \right]$	ζ memory surface shrinkage parameter

memory surface and a larger distance between \mathbf{r} and \mathbf{r}^M in Equations (11)–(12). As clarified in the following, variations in size and position of the memory surface cannot be independent, but it is convenient to address the former aspect prior to the latter. For this purpose, the evolution of m^M is established on a geometrical basis starting from a situation of incipient virgin loading – memory surface coincident or tangent to the yield locus (Figure 2).

Specifically, plastic loading starting from $\boldsymbol{\sigma} \equiv \boldsymbol{\sigma}^M$ is assumed to produce a uniform expansion of the memory surface around the pivot stress point \mathbf{r}_A^M , diametrically opposite to \mathbf{r}^M and kept fixed throughout the process. From an analytical standpoint, this coincides with enforcing the incremental nullity of the memory function f^M at the fixed stress point A (i.e. $d\boldsymbol{\sigma}_A^M = 0$):

$$df^M(\boldsymbol{\sigma}_A^M) = \frac{\partial f^M}{\partial \boldsymbol{\sigma}_A^M} : d\boldsymbol{\sigma}_A^M + \frac{\partial f^M}{\partial \boldsymbol{\alpha}^M} : d\boldsymbol{\alpha}^M + \frac{\partial f^M}{\partial m^M} dm^M = 0 \quad (14)$$

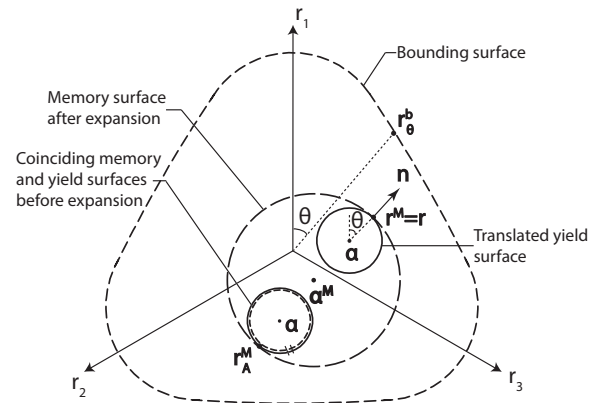


Fig. 2. Memory surface expansion during virgin loading.

Trivial manipulations (see Appendix I) lead to the following relationship:

$$dm^M = \sqrt{\frac{3}{2}} d\boldsymbol{\alpha}^M : \mathbf{n} \quad (15)$$

which is significantly simpler than what obtained by Corti (2016) for a memory surface with non-circular π -section. It is further assumed by analogy that Equation (15) determines the relationship between expansion (dm^M) and translation ($d\boldsymbol{\alpha}^M$) of the memory locus under any loading conditions, not only virgin.

While $dm^M > 0$ (expansion) underlies ‘fabric reinforcement’ and sand stiffening within the expanded memory locus, an opposite effect is usually induced by dilative deformation stages and increase in void ratio (Nemat-Nasser & Tobita, 1982). Such a ‘damage’ to the fabric configuration results in lower sand stiffness. Here, the suggestion by Corti (2016) is followed, and an additional contraction term is cast into Equation (15) to let the memory surface shrink only during dilation (negative $d\varepsilon_{vol}$):

$$dm^M = \sqrt{\frac{3}{2}} d\boldsymbol{\alpha}^M : \mathbf{n} - \frac{m^M}{\zeta} f_{shr} \langle -d\varepsilon_{vol}^p \rangle \quad (16)$$

in which the contraction term on the right is proportional to the current locus size m^M and plastic volumetric strain increment $d\varepsilon_{vol}^p$, with a purely geometrical factor f_{shr} described with more detail in the Appendix I. The contraction rate during dilation is governed by the material parameter ζ , assumed for simplicity not to depend on any stress/state variables (e.g. p , e , etc.).

Memory surface translation

In analogy with the translation rule for the yield locus, the centre of the memory surface is assumed to translate along the direction of $\mathbf{r}_\theta^b - \mathbf{r}^M$ (Figure 1):

$$d\boldsymbol{\alpha}^M = \frac{2}{3} \langle L^M \rangle h^M (\mathbf{r}_\theta^b - \mathbf{r}^M) \quad (17)$$

The hardening law (17) shares the same structure with Equation (8), and requires a method to derive the ‘memory-counterparts’ of the plastic multiplier and the hardening coefficient, namely L^M and h^M . The same approach used for the isotropic memory hardening is re-adopted: the translation rule for $\boldsymbol{\alpha}^M$ is rigorously specified for virgin loading and then extended to any other conditions. Accordingly, analytical derivations and material parameters are substantially reduced in a way proven successful by the the results in the following.

It is assumed that during virgin loading ($\boldsymbol{\sigma} \equiv \boldsymbol{\sigma}^M$) the same magnitude of the incremental plastic strain can be derived by using the yield or memory loci indifferently. The equalities below follow directly (see relevant derivations in the Appendix I):

$$L^M = L$$

$$h^M = \frac{1}{2} \left[\frac{b_0}{(\mathbf{r}^M - \mathbf{r}_{in}) : \mathbf{n}} + \sqrt{\frac{3}{2}} \frac{m^M f_{shr} \langle -D \rangle}{\zeta (\mathbf{r}_\theta^b - \mathbf{r}^M) : \mathbf{n}} \right] \quad (18)$$

and are then extended by analogy to non-virgin loading.

Memory surface: effect on the sand dilation

As a phenomenological recorder of fabric effects, the memory surface is also exploited to enhance the dilatancy factor D in Equation (6), in a new way different from SANISAND04. The goal is to use the memory surface to obtain increased dilatancy (or pore pressure build-up in undrained conditions) upon load reversals following dilative deformation (Dafalias & Manzari, 2004). For this purpose,

the memory surface is handled in combination with the same dilatancy locus defined by Dafalias & Manzari (2004), responsible for the transition from contractive to dilative response:

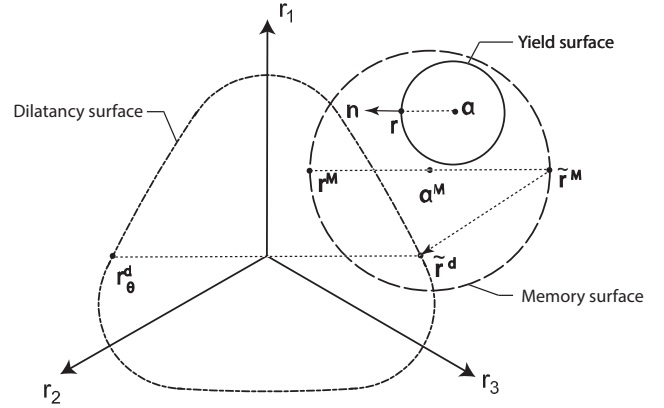


Fig. 3. Geometrical definitions for the enhancement of the dilatancy coefficient.

$$\mathbf{r}_\theta^d = \sqrt{2/3} g(\theta) M \exp(n^d \Psi) \mathbf{n} \quad (19)$$

where the positive parameter n^d governs its evolution towards critical state ($\Psi = 0$). For the sake of clarity, Figure 3 displays certain geometrical quantities associated with the relative position of the memory and dilatancy surfaces. The distance \tilde{b}_d^M is first defined as:

$$\tilde{b}_d^M = (\tilde{\mathbf{r}}^d - \tilde{\mathbf{r}}^M) : \mathbf{n} \quad (20)$$

with $\tilde{\mathbf{r}}^M$ and $\tilde{\mathbf{r}}^d$ projections of \mathbf{r} on the memory and dilatancy surfaces along the $-\mathbf{n}$ direction. When $\tilde{b}_d^M > 0$ the post-dilation contractancy produced by D in Equation (6) is enhanced as follows:

$$D = \left[A_0 \exp \left(\beta \langle \tilde{b}_d^M \rangle / b_{ref} \right) \right] (\mathbf{r}_\theta^d - \mathbf{r}) : \mathbf{n} \quad (21)$$

where A_0 and β are two material parameters. In Equation (21) the exponential term is deactivated by $\tilde{b}_d^M < 0$, that is when the image stress ratio $\tilde{\mathbf{r}}^M$ lies outside the dilatancy surface (i.e. after dilative deformation prior to load reversal). Conversely, additional contractancy arises in the opposite case $\tilde{b}_d^M > 0$ with $\tilde{\mathbf{r}}^M$ lying inside the memory surface. Compared to SANISAND04, the dilatancy coefficient accounts for fabric effects through the same memory locus employed to enhance the plastic modulus coefficient in Equation (11).

CALIBRATION OF CONSTITUTIVE PARAMETERS

The new model requires the calibration of sixteen constitutive parameters, only one more than SANISAND04. Two subsets parameters may be distinguished: the first includes material parameters already present in the original SANISAND04 formulation – namely, from G_0 to n^d in Table 2; the remaining parameters govern directly the (high)-cyclic performance under both drained and undrained loading. The calibration of material parameters is discussed hereafter with reference to the monotonic and cyclic laboratory tests performed by Wichtmann (2005) on a quartz sand – $D_{50} = 0.55$ mm, $D_{10} = 0.29$ mm, $C_u = D_{60}/D_{10} = 1.8$ (non-uniformity index), $e_{max} = 0.874$, $e_{min} = 0.577$. Numerical simulations are executed with yield and memory surfaces initially coincident.

Table 2. Model parameters for the quartz sand tested by Wichtmann (2005)

Elasticity		Critical state					Yield surface	Plastic modulus			Dilatancy		Memory surface		
G_0	ν	M	c	λ_c	e_0	ξ	m	h_0	c_h	n^b	A_0	n^d	μ_0	ζ	β
110	0.05	1.27	0.712	0.049	0.845	0.27	0.01	5.95	1.01	2.0	1.06	1.17	260	0.0005	1

The calibration of the first subset against monotonic tests is based on the procedure detailed in Dafalias & Manzari (2004). The shear modulus G_0 can be derived from the small-strain branch of experimental stress-strain curves, or alternatively from well-established empirical relationships (e.g. Richart *et al.* (1970); Hardin & Black (1966)). A Poisson's ratio equal to 0.05 was assumed following the suggestion of Dafalias & Manzari (2004) for an open-wedge yield surface. Opening of yield surface $m = 0.01$ is also consistent with the SANISAND04 model. The parameters governing the shape of critical state line in the $e - \ln p$ plane (e_0 , λ_c and ξ) and the critical state shear strength (M and c) have been identified by fitting both strength and volumetric strain trends at ultimate conditions for different void ratios and stress levels, as illustrated in Figure 4 by means of deviatoric stress – axial strain ($q - \varepsilon_a$) and volumetric strain – axial strain ($\varepsilon_{vol} - \varepsilon_a$) plots. More details about the calibration of the remaining plastic modulus (h_0 , c_h and n_b) and dilatancy (A_0 and n_d) parameters are available in Dafalias & Manzari (2004) and Taiebat & Dafalias (2008). Due to the limited availability of monotonic tests for the considered quartz sand, these parameters have been determined by fitting the available stress – strain ($q - \varepsilon_a$) and volumetric strain – axial strain ($\varepsilon_{vol} - \varepsilon_a$) trends as shown in Figure 4. All calibrated soil parameters are reported in Table 2.

The new parameters linked to the proposed memory surface (μ_0 , ζ and β) can be identified by best-fitting cyclic test results, possibly from both drained and undrained triaxial cyclic tests. Here, only the drained triaxial cyclic tests documented in Wichtmann (2005) are exploited for calibration purposes, while their impact on the undrained response is qualitatively discussed. In particular, Wichtmann's experiments concern one-way asymmetric cyclic loading performed in two stages (Figure 5): after the initial isotropic consolidation up to $p = p_{in}$, p -constant shearing is first performed to reach the target average stress ratio $\eta^{ave} = q^{ave}/p_{in}$; then, cyclic axial loading at constant radial stress is applied to obtain cyclic variations in deviatoric stress q about the average value q^{ave} , i.e. $q = q^{ave} \pm q^{ampl}$ (Figure 5b). High-cyclic sand parameters are tuned to match the evolution during regular cycles of the accumulated total strain norm ε^{acc} defined as:

$$\varepsilon^{acc} = \sqrt{(\varepsilon_a^{acc})^2 + 2(\varepsilon_r^{acc})^2} = \sqrt{\frac{1}{3}(\varepsilon_{vol}^{acc})^2 + \frac{3}{2}(\varepsilon_q^{acc})^2} \quad (22)$$

where ε_a^{acc} , ε_r^{acc} , ε_q^{acc} and ε_{vol}^{acc} stand for axial, radial, deviatoric and volumetric accumulated strain, respectively.

As illustrated in Figure 6, the ratcheting response of the soil under drained loading is governed by the μ_0 parameter in Equation (11). Figure 6a proves the superior capability of the memory surface formulation to reproduce the transition from ratcheting to shakedown. The gradual sand stiffening occurs in combination with reduced plastic dissipation, as denoted by the decreasing area enclosed by subsequent stress-strain loops. The sensitivity of ε^{acc} to μ_0 is visualised in Figure 6b and exploited to reproduce the experimental data from Wichtmann (2005). μ_0 is in this case set to 260 by fitting the trend of ε^{acc} against number of loading cycles.

Dilatative deformation tend to ‘damage’ the granular fabric and thus erase ‘sand memory’. This granular process is phenomenologically reproduced by the shrinkage of the memory surface, at a rate governed by the parameter ζ in Equation (16). However, the effect of ζ – only relevant to stress paths beyond the dilatative threshold Equation (19) – is most apparent under undrained conditions: larger ζ values reduce the contraction rate of the memory surface and postpone the build-up of positive pore pressure in the post-dilatation unloading regime (Figure 7a). Under drained high-cyclic loading, increasing ζ still promote the aforementioned memory surface contraction, and affect soil ratcheting in the dilatative regime. For the quartz sand tested by Wichtmann (2005), a drained high-cyclic triaxial test with stress path crossing the phase transformation line is selected for the calibration of the memory surface shrinkage parameter ζ . Influence of ζ on the accumulation of the total strain ε^{acc} in Equation (22) is presented in Figure 7b. $\zeta = 0.0005$ has been selected to reproduce the results of high-cyclic drained tests mobilising sand dilation, – see Figure 7b.

The last parameter β appears in the new definition of the dilatancy coefficient D in Equation (21), and mainly controls the post-dilatation reduction of the mean effective stress in undrained tests. Larger β values allow for larger reductions in effective mean pressure, possibly up to full liquefaction (Figure 8a). Since the considered set of drained test results does not support the calibration of β , $\beta = 1$ has been set judiciously with negligible influence on the strain accumulation predicted during drained cyclic tests (see Figure 8b). Although beyond the scope of this work on drained strain accumulation, the marked influence of β on the undrained response is briefly illustrated in Appendix II.

MODEL PREDICTIONS OF DRAINED RATCHETING UNDER DIFFERENT LOADING PATHS

This section overviews the predictive capability of the model against drained high-cyclic test results from the literature. The parameter set in Table 2 is used to simulate sand ratcheting under different cyclic loading conditions, namely triaxial, simple shear and oedometer. All model results have been obtained via single-element FE simulations performed on the OpenSees simulation platform (Mazzoni *et al.*, 2007). The new model with ratcheting control has been implemented starting from the existing SANISAND04 implementation developed at the University of Washington (Ghofrani & Arduino, 2017).

Cyclic triaxial tests

This section considers triaxial test results from Wichtmann (2005), not previously used for parameter calibration. The experimental data concern the same quartz sand and both standard and non-standard triaxial loading.

Standard triaxial loading

The model is first validated against standard triaxial tests of the kind sketched in Figure 5, i.e. with constant radial stress during axial cyclic loading. The drained ratcheting response is predicted at varying p_{in} , e_{in} , η^{ave} and q^{ampl} . Importantly, a large number of cycles $N = 10^4$ is considered,

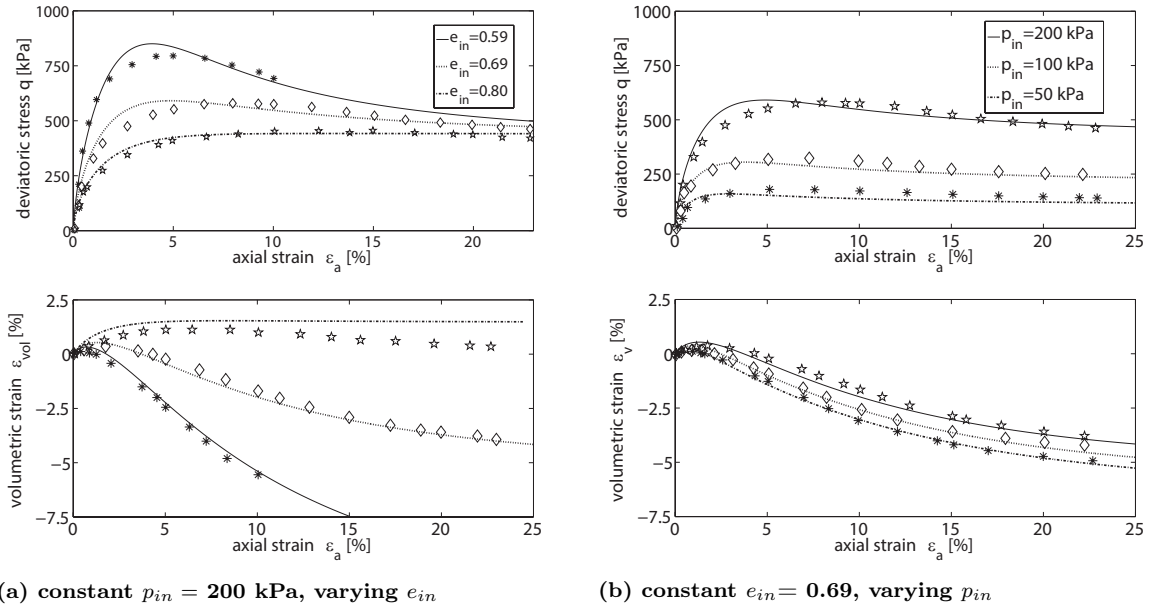


Fig. 4. Calibration of model parameters against the monotonic drained triaxial test results by Wichtmann (2005) – experimental data denoted by markers.

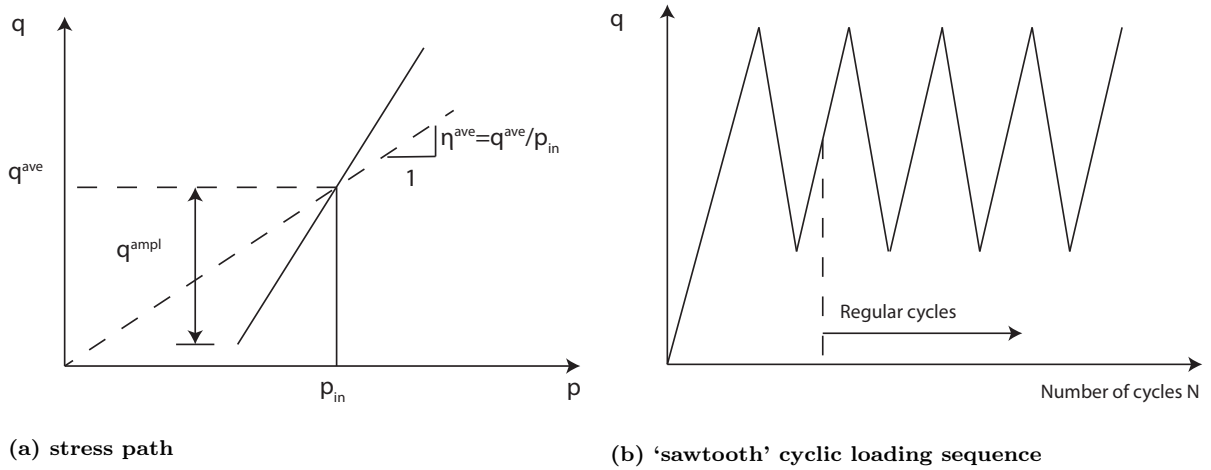


Fig. 5. Stress paths and shear loading sequence in the tests considered for simulation (Wichtmann, 2005).

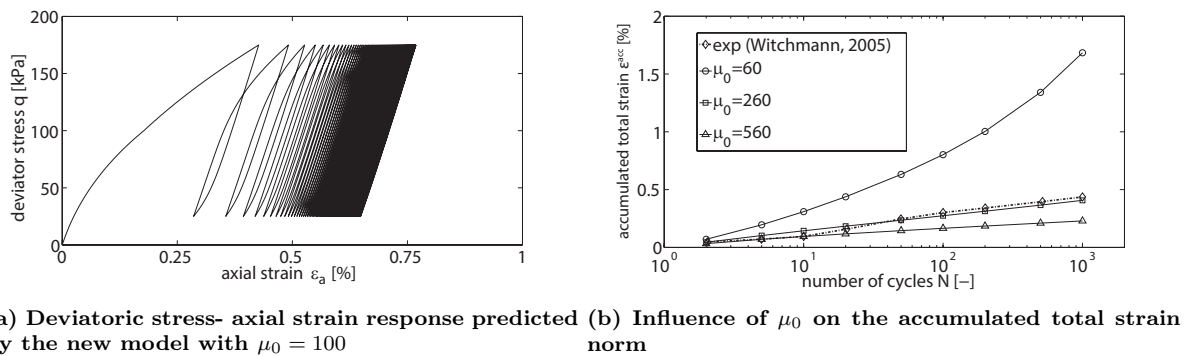
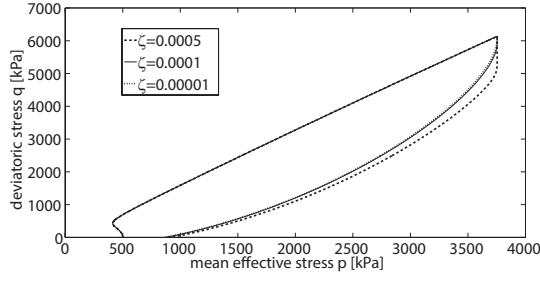


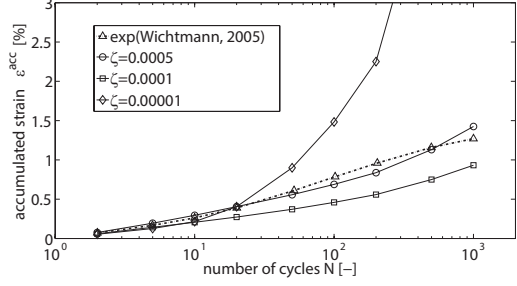
Fig. 6. Influence of μ_0 (Equation (11)) on sand response. The comparison to the experimental data by Wichtmann (2005) refers to the following test/simulation settings: $e_{in} = 0.702$, $q^{ampl} = 60$ kPa, $p_{in} = 200$ kPa, $\eta^{ave} = 0.75$.

and a very satisfactory agreement with experimental data is obtained in most cases.

Influence of initial confining pressure p_{in} The experimental data by Wichtmann (2005) show a quite

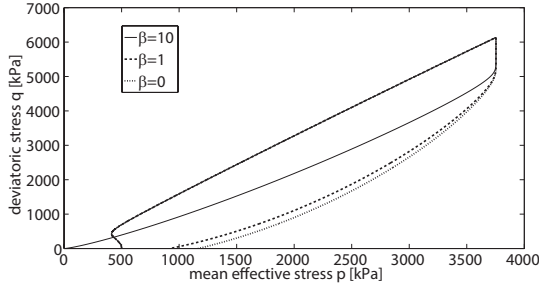


(a) Post-dilation undrained unloading response

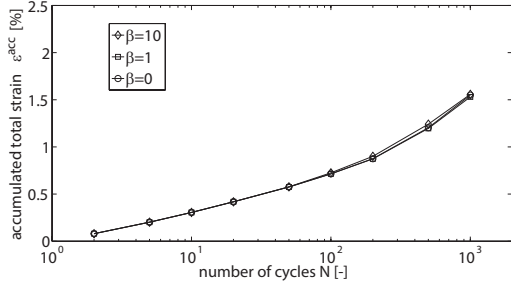


(b) Drained high-cyclic strain accumulation

Fig. 7. Influence of ζ (Equation (16)) on sand response. Simulation settings: (a) $p_{in}=500$ kPa, $e_{in} = 0.6$, load reversal at $\varepsilon_a = 0.07$; (b) $p_{in} = 200$ kPa, $\eta^{ave}=1.125$, $e_{in} = 0.68$, $q^{ampl} = 60$ kPa.



(a) Post-dilation undrained unloading response

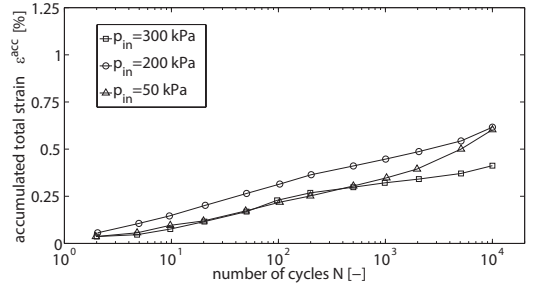


(b) Drained high-cyclic strain accumulation

Fig. 8. Influence of β (Equation (21)) on sand response. Simulation settings: (a) the quartz sand, $p_{in}=500$ kPa, $e_{in} = 0.6$, load reversal at $\varepsilon_a = 0.07$; (b) the quartz sand, $p_{in}=200$ kPa, $\eta^{ave}=1.125$, $e_{in} = 0.68$, $q^{ampl} = 60$ kPa.

low influence of p_{in} on the $\varepsilon^{acc} - N$ curves, especially for $N < 10^4$ (Figure 9a). This is clearly in contrast with what the new model predicts if no pressure-dependence is incorporated in the hardening coefficient h (Equation (11)), i.e. if the exponent n of the p/p_{atm} factor is set to zero (Figure 9b). Conversely, the intrinsic pressure-dependence of SANISAND models can be counterbalanced through a pressure factor $(p/p_{atm})^n$ in h . To avoid a burst in the number of free parameters, a default exponent $n = 1/2$ is adopted, also in agreement with the pressure-dependence typically found for sand stiffness. The comparison between Figures 9a and 9c proves the quantitative suitability of Equation (11).

Influence of initial void ratio e_{in} The experimental evidence from Wichtmann (2005) confirms the intuitive expectation of higher strain accumulation at increasing e_{in} (looser sand specimens). Figure 10 illustrates the potential



(a) Experimental data (Wichtmann, 2005)

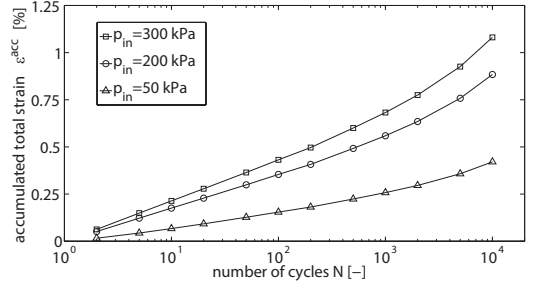
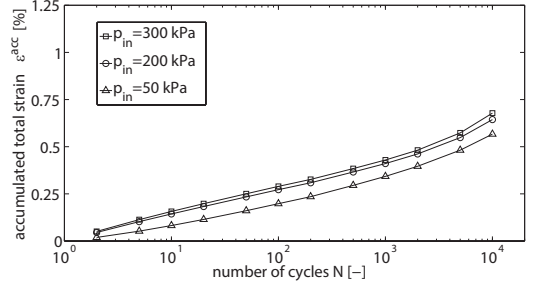
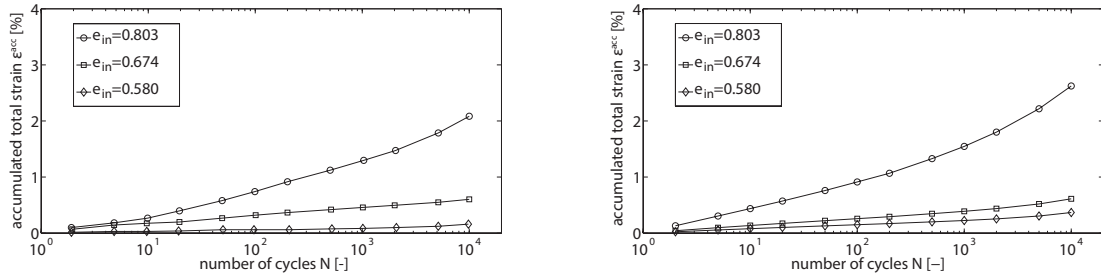
(b) Model simulations: $n = 0$ (c) Model simulations: $n = 1/2$

Fig. 9. Influence of the initial mean pressure p_{in} on cyclic strain accumulation. Test/simulation settings: $e_{in}=0.684$, $\eta^{ave}=0.75$, stress amplitude ratio $\zeta^{ampl} = q^{ampl}/p_{in}=0.3$.

of the new model to capture void ratio effects, though with slight overestimation of ε^{acc} for very dense and very loose specimens. It is worth recalling, however, that the parameters in Table 2 have been calibrated in the remarkable effort to capture relevant response features with a single set of parameters.



(a) Experimental data (Wichtmann, 2005)

(b) Model simulations

Fig. 10. Influence of the initial void ratio e_{in} on cyclic strain accumulation. Test/simulation settings: $p_{in} = 200$ kPa, $\eta^{ave} = 0.75$, $q^{ampl} = 60$ kPa.

Influence of cyclic stress amplitude q^{ampl} The experimental and numerical results in Figure 11 agree on the higher strain accumulation produced by increasing cyclic stress amplitude q^{ampl} . In particular, satisfactory model predictions are shown for medium-dense sand specimens associated with $e_{in} = 0.702$.

Influence of average stress ratio η^{ave} The dependence of sand ratcheting on the average stress obliquity about which stress cycles occur is extremely relevant to practical applications. Indeed, soil elements under/around a foundation experience cyclic loading starting from different stress obliquities, implying different distance from the value related to shear failure.

Figure 12 presents another set of experimental-numerical comparisons at varying average stress ratio η^{ave} . The model can reproduce the experimental increase in strain accumulation rate for larger η^{ave} values, although less accurately as $\eta^{ave} > 1$. Specifically, the simulation with $\eta^{ave} = 1.125$ overestimates ε^{acc} significantly when $N > 1000$: high-cyclic loading at large η^{ave} jeopardises the effectiveness of the memory surface concept, as the model tends again towards the SANISAND04 limit. While near-failure high-cyclic loading seems not too relevant to operational conditions in the field, some concerns could also be raised about the reliability of test measurements performed under such conditions, may be due to strain localisation phenomena (Escribano *et al.*, 2018).

Non-standard triaxial loading

Alternative triaxial loading conditions can be generated by varying both axial and radial stresses during the test. As discussed by Wichtmann (2005), this can produce ‘polarised’ stress-strain cyclic paths, which seem to enhance the tendency to strain accumulation. Unlike most modelling exercises, the model performance is here assessed also in relation to polarised triaxial loading. For this purpose, the following polarisation angle α_{PQ} and amplitude are first defined in the $Q - P$ plane (Figure 13) for direct comparison with Wichtmann’s data:

$$\tan \alpha_{PQ} = \frac{Q^{ampl}}{P^{ampl}} \quad (23)$$

$$S^{ampl} = \sqrt{(P^{ampl})^2 + (Q^{ampl})^2}$$

where $Q = \sqrt{2/3}q$ and $P = \sqrt{3}p$ are isomorphic transformations of the stress invariants p and q , and the superscript ampl denotes cyclic variations about the initial values p^{ave} and q^{ave} .

The model response to non-standard triaxial loading is compared to Wichtmann *et al.*’s experimental data in Figure 14 at varying polarisation angle α_{PQ} , and Figure 15 at varying loading amplitude S^{ampl} . The results in Figure 14 span polarisation angles in the range from 0° to 90° , and show very satisfactory $\varepsilon^{acc} - N$ trends in most cases. The only exception is the case $\alpha_{PQ} = 10^\circ$, in which the model underpredicts the corresponding strain accumulation. This singular outcome is directly caused by the analytical expression (2) of the yield locus, conical and open-ended: in fact, triaxial stress paths at $\alpha_{PQ} = 10^\circ$ happen to be mostly oriented along the uncapped zone of the elastic domain, resulting in underestimated plastic strains.

The effect of the cyclic stress amplitude S^{ampl} at finite polarisation angle ($\alpha_{PQ} = 75^\circ$) can be observed in Figure 15. Strain accumulation is accelerated by increasing S^{ampl} , as testified by simulation results in good agreement with all laboratory data.

Cyclic simple shear tests

Simple shear tests are also well-established in the geo-experimental practice, and allow to explore the soil response to loading paths implying rotation of the principal stress axes. Simple shear loading closely represents conditions relevant to many soil sliding problems, e.g. in the triggering of landslides or in the mobilisation of the shaft capacity of piles.

The experimental work of Wichtmann (2005) also included high-cyclic simple shear tests on the same quartz sand previously tested in the triaxial apparatus – the validity of the same sand parameters in Table 2 can be thus assumed. Two types of cyclic simple shear tests were performed: (i) cyclic shear loading applied along a single direction; (ii) so-called cyclic multidimensional simple shear (CMDSS) tests, in which the direction of shear loading is shifted by 90° in the horizontal plane after, in this case, $N = 1000$ cycles. As all tests were performed under controlled shear strain amplitude, the experimental results were visualised in terms of residual (plastic) strain accumulation – following the definition (22), the residual strain in strain-controlled simple shear tests coincides with the permanent vertical strain.

Experimental and numerical curves corresponding with cyclic shear strain amplitude $\gamma^{ampl} = 5.8 \times 10^{-3}$ are compared in Figure 16, where the dashed lines denote the shift in shear loading direction at $N = 1000$ – relevant to CMDSS tests. Despite unavoidable stress/strain inhomogeneities in simple shear experiments (Dounias & Potts, 1993), reasonably similar residual strain accumulations are displayed in Figures 16a–16b. The

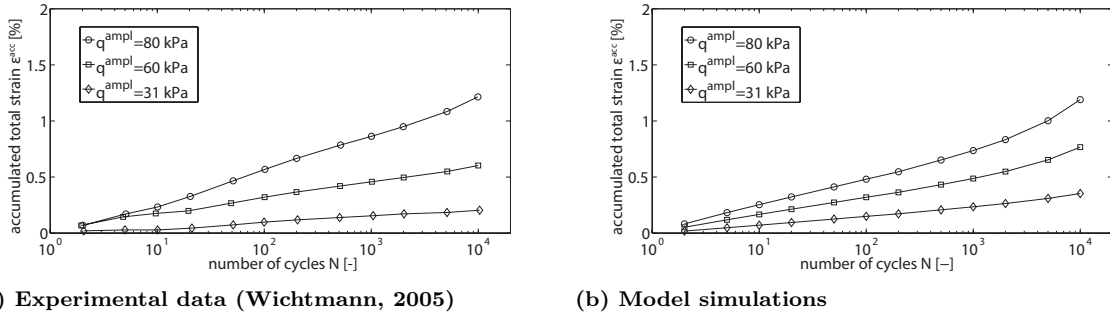


Fig. 11. Influence of the cyclic stress amplitude q^{ampl} on cyclic strain accumulation. Test/simulation settings: $p_{in} = 200$ kPa, $\eta^{ave} = 0.75$, $e_{in} = 0.702$.

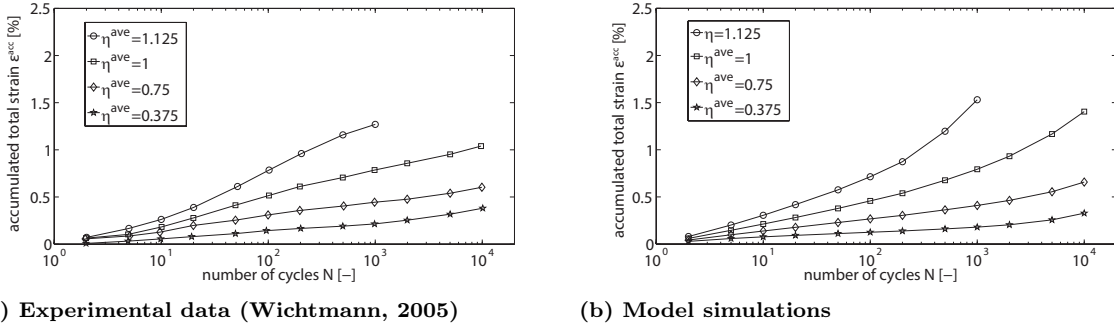


Fig. 12. Influence of the average stress ratio η^{ave} on cyclic strain accumulation. Test/simulation settings: $p_{in} = 200$ kPa, $e_{in} = 0.684$, $q^{ampl} = 60$ kPa.

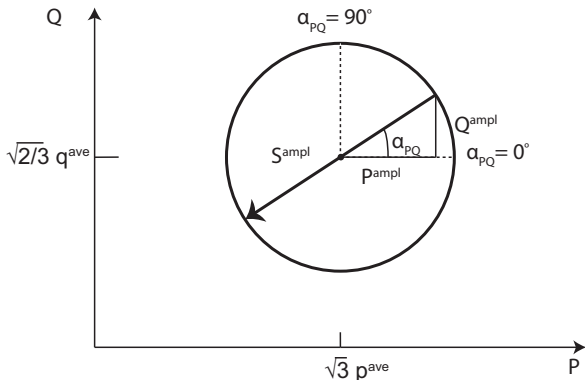


Fig. 13. Non-standard triaxial stress paths in the $Q - P$ plane as defined by Wichtmann (2005).

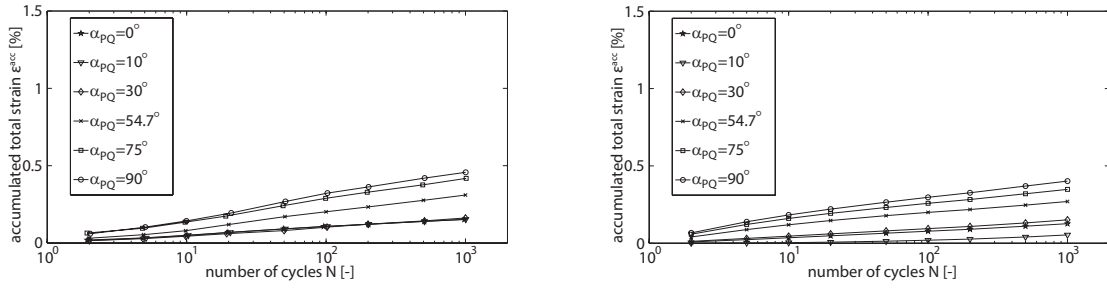
model is also able to capture the temporary increase in accumulation rate produced by the sudden change in shear loading direction.

Cyclic oedometer tests

Cyclic oedometer test results are more rare in the literature, nonetheless a recent instance is reported by Chong & Santamarina (2016) for three different sands (a blasting sand, Ottawa F110 and Ottawa 50–70). The following simulations regard oedometer tests on Ottawa 50–70 specimens ($D_{10} = 0.26$ mm, $D_{50} = 0.33$ mm, $C_u = 1.43$, $e_{max} = 0.87$, $e_{min} = 0.55$) prepared at two different void ratios, $e_{in} = 0.765$ and $e_{in} = 0.645$. Both loose and dense

specimens were subjected to stages of monotonic-cyclic-monotonic loading, at either low or high vertical stress (Figure 17a): (i) *low static load* – monotonic compression up to 100 kPa → cyclic vertical loading in the range 200–100 kPa (100 cycles) → monotonic re-compression up to 1.4 MPa; (ii) *high static load*: monotonic compression up to 1 MPa → cyclic vertical loading in the range 1.1–1 MPa (100 cycles) → monotonic re-compression up to 1.4 MPa. Regarding the data set in Chong & Santamarina (2016), a slightly different calibration approach had to be followed: first, the thirteen SANISAND04 parameters (from G_0 to n^d) have been identified based on drained monotonic triaxial tests on Ottawa sand from the literature (Lin *et al.*, 2015); then, the oedometer high-cyclic response has been simulated by either (i) keeping the same (μ_0, ζ, β) set in Table (Figure 17b), or adjusting the three parameters for best-fit purposes (Figure 17c). Experimental and numerical results are compared in Figure 17 in terms of void ratio vs vertical stress curves, for consistency with the original plots in Chong & Santamarina (2016).

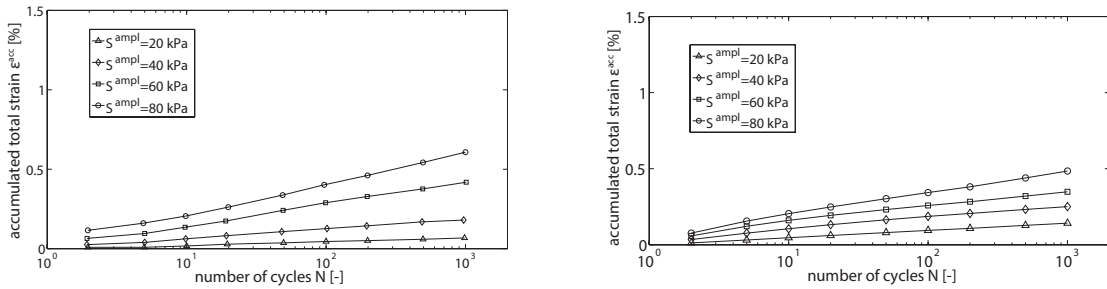
As apparent in Figure 17, most experimental-numerical mismatch is produced during monotonic loading stages, which a model with an open conical yield surface is not suited to reproduce. As for cyclic compaction, the parameters calibrated from Wichtmann's tests tend to underpredict the reduction in void ratio. In contrast, satisfactory numerical results are displayed in Figure 17c after re-calibrating μ_0 and ζ as well (Table 3, same β). There are two steps in re-calibrating μ_0 and ζ : (1) the loose specimen is selected to calibrate μ_0 parameter under the loading condition that cyclic vertical loading in the range 200–100 kPa, since under this condition the parameters ζ and β have no impact on the cyclic behaviour; (2) the dense sample under the same cyclic loading conditions is selected



(a) Experimental data (Wichtmann, 2005)

(b) Model simulations

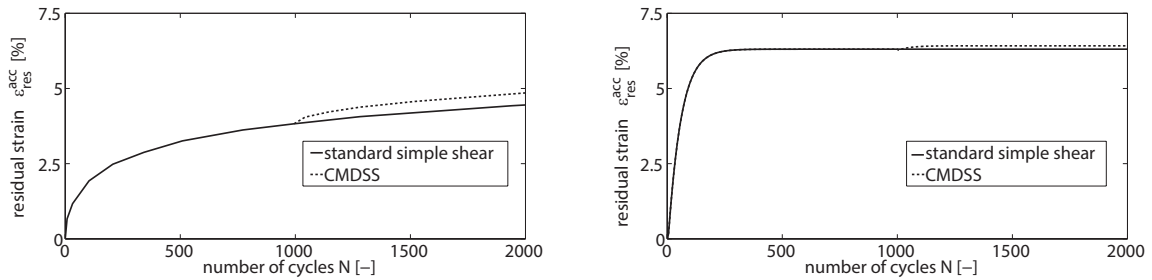
Fig. 14. Influence of the polarisation angle α_{PQ} on cyclic strain accumulation. Test/simulation settings: $p_{in} = 200$ kPa, $e_{in} = 0.69$, $\eta^{ave} = 0.5$, stress amplitude in the $Q - P$ plane $S^{ampl} = 60$ kPa.



(a) Experimental data (Wichtmann, 2005)

(b) Model simulations

Fig. 15. Influence of the stress amplitude S^{ampl} in the $Q - P$ plane on cyclic strain accumulation. Test/simulation settings: $p_{in} = 200$ kPa, $e_{in} = 0.69$, $\eta^{ave} = 0.5$, $\alpha_{PQ} = 75^\circ$.



(a) Experimental results

(b) Simulation results

Fig. 16. Cyclic simple shear tests (single loading direction and CMDSS) – comparison between experimental results and model predictions. Test/simulation settings: $\sigma_a = 24$ kPa (initial vertical stress), $e_{in} = 0.69$, $\gamma^{ampl} = 5.8 \times 10^{-3}$.

Table 3. Model parameters for the Ottawa sand tested by Chong & Santamarina (2016)

Elasticity		Critical state					Yield surface	Plastic modulus			Dilatancy		Memory surface		
G_0	ν	M	c	λ_c	e_0	ξ	m	h_0	c_h	n^b	A_0	n^d	μ_0	ζ	β
90	0.05	1.28	0.8	0.012	0.898	0.7	0.01	5.25	1.01	1.2	0.4	1.35	44	0.005	1

to calibrate ζ with the μ_0 determined in step (1). Other simulations are conducted with the same parameters. The model captures two expected, yet relevant, aspects:

- at given initial vertical stress, the looser sand compact more than the dense sand; for a given initial void ratio, higher initial compression level results in lower cyclic compaction;
- after cyclic loading, the void ratio evolves during re-compression towards the initial virgin compression line (Figure 17c).

The results in Figure 17 confirm the remarkable predictive potential of new model. It could also be shown that fully realistic values of the horizontal-to-vertical stress ratio are obtained, owing to the rotational mechanism of the narrow yield surface (and regardless of the low Poisson's ratio selected – Table 3). The predictions of the monotonic oedometer response could be improved by introducing a capped yield surface as proposed by Taiebat & Dafalias (2008).

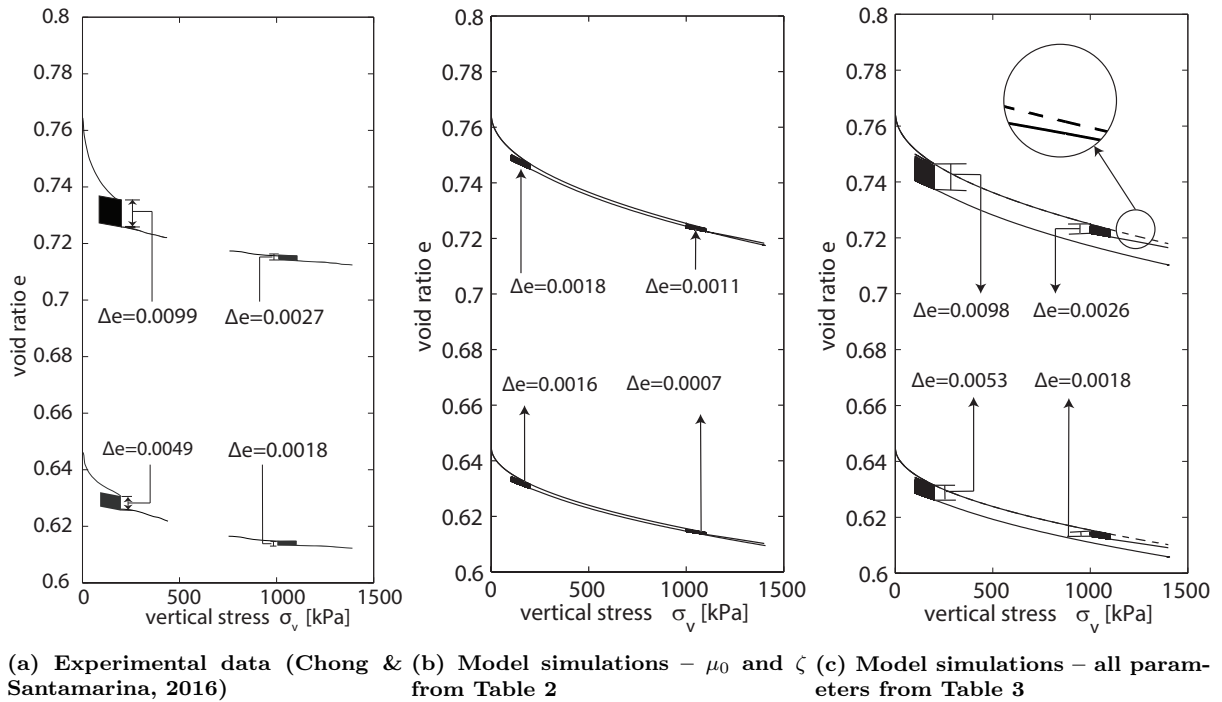


Fig. 17. Cyclic oedometer tests – comparison between experimental results and model predictions.

COMPLIANCE WITH THE CONCEPT OF ‘TERMINAL DENSITY’

While experimental and numerical results were compared above in terms of strain norm ε^{acc} (Equation (22)), it is also interesting to inspect the accumulation of volumetric (ε_{vol}^{acc}) and deviatoric (ε_q^{acc}) strains individually – as exemplified in Figure 18. Based on experimental observations, Wichtmann (2005) concluded that the $\varepsilon_{vol}^{acc}/\varepsilon_q^{acc}$ ratio mainly depends on the average stress ratio η^{ave} held during cyclic loading. Other factors like void ratio, confining pressure and stress amplitude seemed to play limited roles. The new model is found to reproduce such a ratio correctly in the medium/high strain range, although with an overall underestimation of ε_{vol}^{acc} (Figure 18 – note that the experimental and predicted trend lines become parallel for $\varepsilon_q^{acc} > 0.4$).

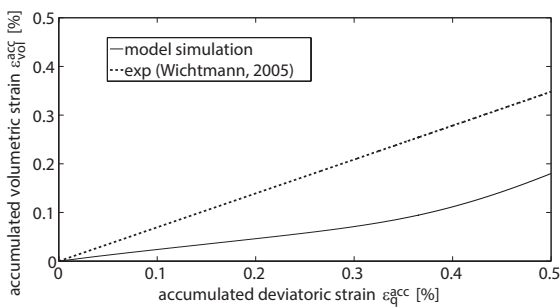


Fig. 18. High-cyclic evolution of deviatoric and volumetric strain under drained triaxial loading. Test/simulation settings: $p_{in} = 200$ kPa, $e_{in} = 0.7$, $\eta^{ave} = 0.75$, $q^{ampl} = 60$ kPa, $N = 10^4$.

It is believed that these inaccuracies relate mostly to the assumed modelling of sand dilatancy, future efforts will be spent to remedy this shortcoming. However, it is also worth reflecting here on the link between Wichtmann’s results and

other related published results. In particular, Narsilio & Santamarina (2008) postulated on an experimental basis the existence of a so-called ‘terminal density’, that is a state of constant void ratio and steady fabric – including critical state as a particular instance. Every sand appears to attain a specific terminal density depending on initial, boundary and loading conditions (Narsilio & Santamarina, 2008; Chong & Santamarina, 2016), with direct influence on the observed accumulation of all strain components. However, the experimental trend in Figure 18 from Wichtmann (2005) does not seem to evolve towards such a terminal state. Further studies about such a discrepancy and, more widely, about the existence and the properties of terminal density loci will positively affect future modelling efforts on the high-cyclic response of soils.

CONCLUSIONS

The critical state, bounding surface SANISAND04 model was endowed with an additional locus in the stress space (memory surface) to improve the simulation of high-cyclic sand ratcheting under a variety of initial, boundary and loading conditions. The constitutive equations, directly presented in a multi-axial framework, were implemented in the finite element code OpenSees, based on an existing, open-source implementation of SANISAND04. Compared to previous formulations, the proposed models proved more reliable in capturing the dependence of sand ratcheting, as well as potentially more flexible in terms of mean effective pressure decay under undrained loading. Extensive validation against experimental results was performed with regard to triaxial (standard and non-standard), simple shear and oedometer drained cyclic tests.

The impact of this and future work on the subject will link to further calibration efforts against new high-cyclic datasets, still rare in the scientific literature and usually out of the scope of industry projects. It is anticipated that deeper insight and more reliable empirical correlations

may be obtained for a range of sandy materials. This will support the use of ratcheting models, both implicit and explicit, in the (likely) lack of specific evidence about strain accumulation trends.

NOTATIONS

A_0	‘intrinsic’ dilatancy parameter
\tilde{b}_d^M	relative position of the memory and the dilatancy surfaces
b^M	yield-to-memory surface distance
b_0	hardening factor
b_{ref}	reference distance for normalisation
C_u	uniformity coefficient
c	compression-to-extension strength ratio
c_h	hardening parameter
D	dilatancy coefficient
$D_{10,50,60}$	the diameter in the particle-size distribution curve corresponding to 10%, 50% and 60% finer
\mathbf{e}	deviatoric strain tensor
e	void ratio
e_0	reference critical void ratio in Equation 3
e_c	void ratio at critical state
e_{in}	initial void ratio
f	yield function
f^M	memory function
f_{shr}	memory surface shrinkage geometrical factor
G	shear modulus
G_0	dimensionless shear modulus
$g(\theta)$	interpolation function for Lode angle dependence
\tilde{h}	virgin state hardening factor generalised into common situations
h	hardening factor
h^M	memory-counterpart of the hardening coefficient
h_0	hardening parameter
\mathbf{I}	second-order identity tensor
K_p	plastic modulus
K_p^M	memory-counterpart of the plastic modulus
L	plastic multiplier
L^M	memory-counterpart of the plastic multiplier
M	critical stress ratio in compression
m	yield locus opening parameter
m^M	memory locus opening parameter
N	number of loading cycles
\mathbf{n}	unit tensor normal to the yield locus
\mathbf{n}^M	unit tensor for memory surface contraction
n	pre-set material parameter
$n^{b,d}$	void ratio dependence parameters
P	isomorphic transformation of the stress invariant p
P^{ampl}	cyclic amplitude of P
p	mean effective stress
p_{atm}	atmospheric pressure
p_{in}	initial effective mean stress
Q	isomorphic transformation of the stress invariant q
Q^{ampl}	cyclic amplitude of Q
q	deviatoric stress
q^{ampl}	cyclic deviatoric stress amplitude
q^{ave}	average deviatoric stress
\mathbf{R}'	deviatoric plastic flow direction tensor

\mathbf{R}	plastic strain rate direction tensor
\mathbf{r}	deviatoric stress ratio tensor
\mathbf{r}^M	image deviatoric stress ratio point on the memory locus
$\mathbf{r}_{\theta+\pi}^b$	projection onto the bounding surface with relative Lode angle $\theta + \pi$
$\mathbf{r}_{\theta}^{b,c,d}$	bounding, critical and dilatancy deviatoric stress ratio tensor
$\mathbf{r}_{C,D}$	projection of \mathbf{r} along $-\mathbf{n}^M$ on memory surfaces after and before contraction
\mathbf{r}_{in}	initial load-reversal tensor
$\tilde{\mathbf{r}}$	projection of \mathbf{r} on the yield surface along $-\mathbf{n}$
$\tilde{\mathbf{r}}^M$	projection of \mathbf{r} on the memory surface along $-\mathbf{n}$
$\tilde{\mathbf{r}}^d$	projection of \mathbf{r} on the dilatancy surface along $-\mathbf{n}$
S^{ampl}	cyclic polarisation stress amplitude
\mathbf{s}	deviatoric stress tensor
w	pre-set material parameter
$x_{1,2,3}$	line-segments defined to derive memory surface contraction law
α_{PQ}	polarisation angle
$\boldsymbol{\alpha}$	back-stress ratio tensor
$\boldsymbol{\alpha}^M$	memory back-stress ratio tensor
β	dilatancy memory parameter
$\boldsymbol{\varepsilon}$	strain tensor
ε^{acc}	accumulated total strain
$\varepsilon_{a,r,q,vol}^{acc}$	accumulated axial, radial, deviatoric and volumetric strain
$\varepsilon_{a,vol}$	axial and volumetric strains
ε_{vol}^p	plastic volumetric strain
η^{ave}	average deviatoric stress ratio in triaxial space
γ^{ampl}	cyclic shear strain amplitude
λ_c	CSL shape parameter
μ_0	ratcheting parameter
ν	Poisson’s ratio
Ψ	state parameter
$\boldsymbol{\sigma}$	stress tensor
$\boldsymbol{\sigma}^M$	image stress tensor on the memory locus
$\boldsymbol{\sigma}_A^M$	stress tensor at point A
ζ^{ampl}	cyclic stress amplitude ratio
θ	relative Lode angle
ξ	CSL shape parameter
ζ	memory surface shrinkage parameter

REFERENCES

- Abadie, C. N. (2015). *Cyclic lateral loading of monopile foundations in cohesionless soils*. Ph.D. thesis, University of Oxford.
- Achmus, M., Kuo, Y.-S. & Abdel-Rahman, K. (2009). Behavior of monopile foundations under cyclic lateral load. *Computers and Geotechnics* **36**, No. 5, 725–735.
- Alonso-Marroquin, F. & Herrmann, H. (2004). Ratcheting of granular materials. *Physical Review Letters* **92**, No. 5, 054301.
- Andersen, K. (2015). Cyclic soil parameters for offshore foundation design. *Frontiers in Offshore Geotechnics III* **5**.
- Andersen, K. H. (2009). Bearing capacity under cyclic loading — offshore, along the coast, and on land. The 21st Bjerrum Lecture presented in Oslo, 23 November 2007. *Canadian Geotechnical Journal* **46**, No. 5, 513–535, doi:10.1139/T09-003.
- Andresen, L., Petter Jostad, H. & Andersen, K. H. (2010). Finite element analyses applied in design of foundations

- and anchors for offshore structures. *International Journal of Geomechanics* **11**, No. 6, 417–430.
- Been, K. & Jefferies, M. G. (1985). A state parameter for sands. *Géotechnique* **35**, No. 2, 99–112.
- Calvetti, F. & di Prisco, C. (2010). Discrete numerical investigation of the ratcheting phenomenon in granular materials. *Comptes Rendus Mecanique* **338**, No. 10-11, 604–614.
- Chong, S.-H. (2017). Numerical simulation of offshore foundations subjected to repetitive loads. *Ocean Engineering* **142**, 470–477.
- Chong, S.-H. & Santamarina, J. C. (2016). Sands subjected to repetitive vertical loading under zero lateral strain: accumulation models, terminal densities, and settlement. *Canadian Geotechnical Journal* **53**, No. 12, 2039–2046.
- Chow, S., O’Loughlin, C., Corti, R., Gaudin, C. & Diambra, A. (2015). Drained cyclic capacity of plate anchors in dense sand: Experimental and theoretical observations. *Géotechnique Letters* **5**, No. 2, 80–85.
- Corciulo, S., Zanoli, O. & Pisanò, F. (2017). Transient response of offshore wind turbines on monopiles in sand: role of cyclic hydro-mechanical soil behaviour. *Computers and Geotechnics* **83**, 221–238.
- Corti, R. (2016). *Hardening memory surface constitutive model for granular soils under cyclic loading*. Ph.D. thesis, University of Bristol.
- Corti, R., Diambra, A., Muir Wood, D., Escribano, D. E. & Nash, D. F. (2016). Memory surface hardening model for granular soils under repeated loading conditions. *Journal of Engineering Mechanics*, 04016102.
- Corti, R., Gourvenec, S. M., Randolph, M. F. & Diambra, A. (2017). Application of a memory surface model to predict whole-life settlements of a sliding foundation. *Computers and Geotechnics* **88**, 152–163.
- Dafalias, Y. & Taiebat, M. (2016). SANISAND-Z: zero elastic range sand plasticity model. *Géotechnique* **66**, No. 12, 999–1013.
- Dafalias, Y. F. (1986). Bounding surface plasticity. i: Mathematical foundation and hypoplasticity. *Journal of Engineering Mechanics* **112**, No. 9, 966–987.
- Dafalias, Y. F. & Manzari, M. T. (2004). Simple plasticity sand model accounting for fabric change effects. *Journal of Engineering mechanics* **130**, No. 6, 622–634.
- Di Benedetto, H., Blanc, M., Tiouajni, S. & Ezaoui, A. (2014). Elastoplastic model with loading memory surfaces (lms) for monotonic and cyclic behaviour of geomaterials. *International Journal for Numerical and Analytical Methods in Geomechanics* **38**, No. 14, 1477–1502.
- di Prisco, C. & Mortara, G. (2013). A multi-mechanism constitutive model for plastic adaption under cyclic loading. *International Journal for Numerical and Analytical Methods in Geomechanics* **37**, No. 18, 3071–3086.
- di Prisco, C. G. & Muir Wood, D. (2012). *Mechanical behaviour of soils under environmentally-induced cyclic loads*, vol. 534. Springer Science & Business Media.
- Dounias, G. T. & Potts, D. M. (1993). Numerical analysis of drained direct and simple shear tests. *Journal of Geotechnical Engineering* **119**, No. 12, 1870–1891.
- Escribano, D., Nash, D. T. F. & Diambra, A. (2018). Local and global volumetric strain comparison in sand specimens subjected to drained cyclic and monotonic triaxial compression loading. *Geotechnical Testing Journal* **accepted for publication**.
- Gajo, A. & Muir Wood, D. (1999a). A kinematic hardening constitutive model for sands: the multiaxial formulation. *International Journal for Numerical and Analytical Methods in Geomechanics* **23**, No. 9, 925–965.
- Gajo, A. & Muir Wood, D. (1999b). Severn-Trent sand: a kinematic hardening constitutive model for sands: the q-p formulation. *Géotechnique* **49**, No. 5, 595–614.
- Gao, Z. & Zhao, J. (2015). Constitutive modeling of anisotropic sand behavior in monotonic and cyclic loading. *Journal of Engineering Mechanics* **141**, No. 8, 04015017.
- Ghofrani, A. & Arduino, P. (2017). Prediction of LEAP centrifuge test results using a pressure-dependent bounding surface constitutive model. *Soil Dynamics and Earthquake Engineering*.
- Gudehus, G., Amorosi, A., Gens, A., Herle, I., Kolymbas, D., Mašin, D., Muir Wood, D., Niemunis, A., Nova, R., Pastor, M. *et al.* (2008). The soilmodels. info project. *International Journal for Numerical and Analytical Methods in Geomechanics* **32**, No. 12, 1571–1572.
- Hardin, B. O. & Black, W. L. (1966). Sand stiffness under various triaxial stresses. *Journal of Soil Mechanics & Foundations Div* **92**, No. ASCE# 4712 Proceeding.
- Houlsby, G., Abadie, C., Beuckelaers, W. & Byrne, B. (2017). A model for nonlinear hysteretic and ratcheting behaviour. *International Journal of Solids and Structures* **120**, 67–80.
- Ishihara, K., Tatsuoka, F. & Yasuda, S. (1975). Undrained deformation and liquefaction of sand under cyclic stresses. *Soils and foundations* **15**, No. 1, 29–44.
- Jafarzadeh, F., Javaheri, H., Sadek, T. & Muir Wood, D. (2008). Simulation of anisotropic deviatoric response of hostun sand in true triaxial tests. *Computers and Geotechnics* **35**, No. 5, 703–718.
- Jostad, H., Grimstad, G., Andersen, K., Saue, M., Shin, Y. & You, D. (2014). A fe procedure for foundation design of offshore structures—applied to study a potential owt monopile foundation in the korean western sea. *Geotechnical Engineering Journal of the SEAGS & AGSSEA* **45**, No. 4, 63–72.
- Jostad, H., Grimstad, G., Andersen, K. & Sivasithamparam, N. (2015). A FE procedure for calculation of cyclic behaviour of offshore foundations under partly drained conditions. *Frontiers in Offshore Geotechnics III*, 153–172.
- Kan, M. E., Taiebat, H. A. & Khalili, N. (2013). Simplified mapping rule for bounding surface simulation of complex loading paths in granular materials. *International Journal of Geomechanics* **14**, No. 2, 239–253.
- Khalili, N., Habte, M. & Valliappan, S. (2005). A bounding surface plasticity model for cyclic loading of granular soils. *International journal for numerical methods in engineering* **63**, No. 14, 1939–1960.
- LeBlanc, C., Houlsby, G. & Byrne, B. (2010). Response of stiff piles in sand to long-term cyclic lateral loading. *Geotechnique* **60**, No. 2, 79–90.
- Lekarp, F., Isacsson, U. & Dawson, A. (2000). State of the art. ii: Permanent strain response of unbound aggregates. *Journal of transportation engineering* **126**, No. 1, 76–83.
- Li, X. & Dafalias, Y. F. (2000). Dilatancy for cohesionless soils. *Geotechnique* **50**, No. 4, 449–460.
- Li, X. S. & Dafalias, Y. F. (2011). Anisotropic critical state theory: role of fabric. *Journal of Engineering Mechanics* **138**, No. 3, 263–275.
- Li, X.-S. & Wang, Y. (1998). Linear representation of steady-state line for sand. *Journal of geotechnical and geoenvironmental engineering* **124**, No. 12, 1215–1217.
- Lin, H., Suleiman, M. T., Brown, D. G. & Kavazanjian Jr, E. (2015). Mechanical behavior of sands treated by microbially induced carbonate precipitation. *Journal of Geotechnical and Geoenvironmental Engineering* **142**, No. 2, 04015066.
- Liu, H., Zou, D. & Liu, J. (2014). Constitutive modeling of dense gravelly soils subjected to cyclic loading. *International Journal for Numerical and Analytical Methods in Geomechanics* **38**, No. 14, 1503–1518.
- Loukidis, D. & Salgado, R. (2009). Modeling sand response using two-surface plasticity. *Computers and Geotechnics* **36**, No. 1, 166–186.
- Maleki, M., Cambou, B. & Dubujet, P. (2009). Development in modeling cyclic loading of sands based on kinematic hardening. *International journal for numerical and analytical methods in geomechanics* **33**, No. 14, 1641–1658.
- Manzari, M. T. & Dafalias, Y. F. (1997). A critical state two-surface plasticity model for sands. *Géotechnique* **47**, No. 2, 255–272, doi:10.1680/geot.1997.47.2.255.
- Mazzoni, S., McKenna, F., Scott, M. & Fenves, G. (2007). *Opensees command language manual*.

- McNamara, S., García-Rojo, R. & Herrmann, H. J. (2008). Microscopic origin of granular ratcheting. *Physical Review E* **77**, No. 3, 031304.
- Muir Wood, D. & Belkheir, K. (1994). Strain softening and state parameter for sand modelling. *Géotechnique* **44**, No. 2, 335–339.
- Narsilio, A. & Santamarina, J. (2008). Terminal densities. *Geotechnique* **58**, No. 8, 669.
- Nemat-Nasser, S. (2000). A micromechanically-based constitutive model for frictional deformation of granular materials. *Journal of the Mechanics and Physics of Solids* **48**, No. 6, 1541–1563.
- Nemat-Nasser, S. & Tobita, Y. (1982). Influence of fabric on liquefaction and densification potential of cohesionless sand. *Mechanics of Materials* **1**, No. 1, 43–62.
- Niemunis, A., Wichtmann, T. & Triantafyllidis, T. (2005). A high-cycle accumulation model for sand. *Computers and geotechnics* **32**, No. 4, 245–263.
- Oda, M., Nemat-Nasser, S. & Konishi, J. (1985). Stress-induced anisotropy in granular masses. *Soils and foundations* **25**, No. 3, 85–97.
- O’Sullivan, C. & Cui, L. (2009). Micromechanics of granular material response during load reversals: combined DEM and experimental study. *Powder Technology* **193**, No. 3, 289–302.
- O’Sullivan, C., Cui, L. & O’Neill, S. C. (2008). Discrete element analysis of the response of granular materials during cyclic loading. *Soils and Foundations* **48**, No. 4, 511–530.
- Papadimitriou, A. G. & Bouckovalas, G. D. (2002). Plasticity model for sand under small and large cyclic strains: a multiaxial formulation. *Soil Dynamics and Earthquake Engineering* **22**, No. 3, 191–204.
- Papadimitriou, A. G., Bouckovalas, G. D. & Dafalias, Y. F. (2001). Plasticity model for sand under small and large cyclic strains. *Journal of Geotechnical and Geoenvironmental Engineering* **127**, No. 11, 973–983.
- Papadimitriou, A. G., Dafalias, Y. F. & Yoshimine, M. (2005). Plasticity modeling of the effect of sample preparation method on sand response. *Soils and foundations* **45**, No. 2, 109–123.
- Pasten, C., Shin, H. & Santamarina, J. C. (2013). Long-term foundation response to repetitive loading. *Journal of Geotechnical and Geoenvironmental Engineering* **140**, No. 4, 04013036.
- Pisanò, F. & Gavin, K. G. (2017). General report for TC209 - Offshore Geotechnics. In *19th International Conference on Soil Mechanics and Geotechnical Engineering (ICSMGE2017)*, International Society of Soil Mechanics and Geotechnical Engineering (ISSMGE).
- Pisanò, F. & Jeremić, B. (2014). Simulating stiffness degradation and damping in soils via a simple visco-elastic-plastic model. *Soil Dynamics and Earthquake Engineering* **63**, 98–109.
- Randolph, M. & Gourvenec, S. (2011). *Offshore geotechnical engineering*. CRC Press.
- Richart, F., Hall, J. & Woods, R. (1970). *Vibrations of soils and foundations*. N.J.
- Stallebrass, S. & Taylor, R. (1997). The development and evaluation of a constitutive model for the prediction of ground movements in overconsolidated clay. *Géotechnique* **47**, 235–253.
- Suiker, A. S. & de Borst, R. (2003). A numerical model for the cyclic deterioration of railway tracks. *International journal for numerical methods in engineering* **57**, No. 4, 441–470.
- Suiker, A. S., Selig, E. T. & Frenkel, R. (2005). Static and cyclic triaxial testing of ballast and subballast. *Journal of geotechnical and geoenvironmental engineering* **131**, No. 6, 771–782.
- Taiebat, M. & Dafalias, Y. F. (2008). Sanisand: Simple anisotropic sand plasticity model. *International Journal for Numerical and Analytical Methods in Geomechanics* **32**, No. 8, 915–948.
- Tasiopoulou, P. & Gerolymos, N. (2016). Constitutive modeling of sand: Formulation of a new plasticity approach. *Soil Dynamics and Earthquake Engineering* **82**, 205–221.
- Triantafyllidis, T., Wichtmann, T., Chrisopoulos, S., Zachert, H. et al. (2016). Prediction of long-term deformations of offshore wind power plant foundations using engineer-oriented models based on HCA. In *The 26th International Ocean and Polar Engineering Conference*, International Society of Offshore and Polar Engineers.
- Wan, R. G. & Guo, J. (2001). Drained cyclic behavior of sand with fabric dependence. *Journal of Engineering mechanics* **127**, No. 11, 1106–1116.
- Wichtmann, T. (2005). *Explicit accumulation model for non-cohesive soils under cyclic loading*. Ph.D. thesis, Inst. für Grundbau und Bodenmechanik Bochum University, Germany.
- Wichtmann, T., Niemunis, A. & Triantafyllidis, T. (2005). Strain accumulation in sand due to cyclic loading: drained triaxial tests. *Soil Dynamics and Earthquake Engineering* **25**, No. 12, 967–979.
- Wichtmann, T., Niemunis, A. & Triantafyllidis, T. (2007). On the influence of the polarization and the shape of the strain loop on strain accumulation in sand under high-cyclic loading. *Soil Dynamics and Earthquake Engineering* **27**, No. 1, 14–28.
- Wichtmann, T., Niemunis, A. & Triantafyllidis, T. (2010). Towards the FE prediction of permanent deformations of offshore wind power plant foundations using a high-cycle accumulation model. In *International Symposium: Frontiers in Offshore Geotechnics, Perth, Australia*, pp. 635–640.
- Wichtmann, T., Niemunis, A. & Triantafyllidis, T. (2015). Improved simplified calibration procedure for a high-cycle accumulation model. *Soil Dynamics and Earthquake Engineering* **70**, 118–132.
- Wichtmann, T. & Triantafyllidis, T. (2015). Inspection of a high-cycle accumulation model for large numbers of cycles (N= 2 million). *Soil Dynamics and Earthquake Engineering* **75**, 199–210.
- Zhao, J. & Guo, N. (2013). Unique critical state characteristics in granular media considering fabric anisotropy. *Géotechnique* **63**, No. 8, 695.

APPENDIX I – ANALYTICAL DERIVATIONS

This appendix collects relevant analytical derivations, skipped in the main text for better readability.

Memory surface expansion

The expansion law for the memory surface is derived through the consistency condition in Equation (14) applied to the stress point A (Figure 2). Importantly, the partial derivative $\partial f^M / \partial \boldsymbol{\alpha}^M$ at point A can be expressed as follows:

$$\left. \frac{\partial f^M}{\partial \boldsymbol{\alpha}^M} \right|_A = -p \frac{\mathbf{r}_A^M - \boldsymbol{\alpha}^M}{\sqrt{(\mathbf{r}_A^M - \boldsymbol{\alpha}^M) : (\mathbf{r}_A^M - \boldsymbol{\alpha}^M)}} = p\mathbf{n} \quad (\text{A1})$$

due to the position of A taken diametrically opposed to the projection of the stress point on the memory surface (see Figure 2, along $-\mathbf{n}$). After computing the derivative $\partial f^M / \partial m^M$ and setting $d\boldsymbol{\sigma}_A^M = 0$, the evolution law (15) results from Equation (14).

Memory surface contraction

The geometrical factor f_{shr} in Equation 16 is evaluated to prevent the memory surface from shrinking smaller than the elastic domain.

It is assumed that the shrinkage of the memory surface occurs at fixed image stress ratio \mathbf{r}^M , along the direction of the unit tensor \mathbf{n}^M :

$$\mathbf{n}^M = \frac{\mathbf{r}^M - \mathbf{r}}{\sqrt{(\mathbf{r}^M - \mathbf{r}) : (\mathbf{r}^M - \mathbf{r})}} \quad (\text{A2})$$

The following segments along the \mathbf{n}^M directions are defined in agreement with in Figure A1:

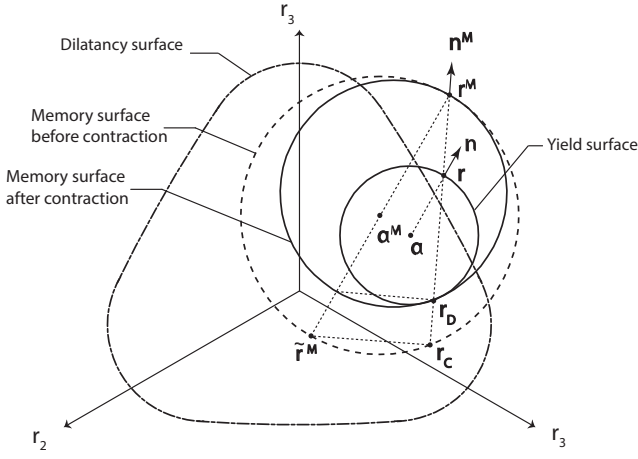


Fig. A1. Geometrical contraction mechanism of the memory surface.

$$\begin{aligned} x_1 &= \mathbf{n}^M : (\mathbf{r}^M - \mathbf{r}) \\ x_2 &= \mathbf{n}^M : (\mathbf{r} - \mathbf{r}_D) = \mathbf{n}^M : (\mathbf{r} - \tilde{\mathbf{r}}) \\ x_3 &= \mathbf{n}^M : (\mathbf{r}^M - \mathbf{r}_C) = \mathbf{n}^M : (\mathbf{r}^M - \tilde{\mathbf{r}}^M) \end{aligned} \quad (\text{A3})$$

where

$$\tilde{\mathbf{r}} = \boldsymbol{\alpha} - \sqrt{2/3} m \mathbf{n} \quad \tilde{\mathbf{r}}^M = \boldsymbol{\alpha}^M - \sqrt{2/3} m^M \mathbf{n} \quad (\text{A4})$$

It should be recalled that, during virgin loading, $\mathbf{r}^M = \mathbf{r}$ and $\mathbf{n}^M = \mathbf{n}$. To avoid undesired intersections, the contraction of the memory surface is gradually decelerated as the yield-memory tangency is approached. For this purpose, the factor f_{shr} in Equation 16 is defined as per Corti (2016):

$$f_{shr} = 1 - \frac{x_1 + x_2}{x_3} \quad (\text{A5})$$

Under general conditions, points C and D do not coincide, so that the segment x_3 is longer than segment $x_1 + x_2$. Therefore, $(x_1 + x_2)/x_3 < 1 \Rightarrow f_{shr} > 0$ and the contraction mechanism is carried on until the segment CD vanishes.

Memory surface translation

As postulated in the relevant section, it is assumed that during virgin loading ($\boldsymbol{\sigma} \equiv \boldsymbol{\sigma}^M$) the same magnitude of the incremental plastic strain can be derived by using the yield or memory loci indifferently:

$$\frac{\|d\boldsymbol{\varepsilon}^p\|}{\|\mathbf{R}\|} = L = \left(\frac{1}{K_p} \frac{\partial f}{\partial \boldsymbol{\sigma}} : d\boldsymbol{\sigma} \right) = \left(\frac{1}{K_p^M} \frac{\partial f^M}{\partial \boldsymbol{\sigma}^M} : d\boldsymbol{\sigma}^M \right) = L^M \quad (\text{A6})$$

where $\mathbf{R} = \mathbf{R}' + D\mathbf{I}/3$ (see Equation (6)). Under virgin loading conditions, $L^M = L$ and $K_p^M = K_p$ hold rigorously.

By enforcing plastic consistency on the memory surface, it can be found that:

$$\frac{\partial f^M}{\partial \boldsymbol{\sigma}^M} : d\boldsymbol{\sigma}^M = - \left(\frac{\partial f^M}{\partial \boldsymbol{\alpha}^M} : d\boldsymbol{\alpha}^M + \frac{\partial f^M}{\partial m^M} dm^M \right) = L^M K_p^M \quad (\text{A7})$$

After setting $L = L^M$ and substituting the partial derivatives of the memory function f^M with respect to $\boldsymbol{\alpha}^M$ and m^M , Equation A7 can be rewritten as:

$$L K_p^M = p \mathbf{n} : d\boldsymbol{\alpha}^M + \sqrt{\frac{2}{3}} p dm^M \quad (\text{A8})$$

Introducing Equation (17) into the above equation leads to:

$$K_p^M = \frac{2}{3} p \left[h^M (\mathbf{r}_\theta^b - \mathbf{r}^M) : \mathbf{n} + \sqrt{\frac{3}{2}} \frac{1}{L} dm^M \right] \quad (\text{A9})$$

Imposing virgin loading ($\mathbf{r} = \mathbf{r}^M$) into Equation (8) yields:

$$K_p = \frac{2}{3} p h (\mathbf{r}_\theta^b - \mathbf{r}) : \mathbf{n} = \frac{2}{3} p \tilde{h} (\mathbf{r}_\theta^b - \mathbf{r}^M) : \mathbf{n} \quad (\text{A10})$$

with

$$\tilde{h} = \frac{b_0}{(\mathbf{r}^M - \mathbf{r}_{in}) : \mathbf{n}} \quad (\text{A11})$$

Under virgin loading conditions, $K_p^M = K_p$. Combining Equation A9 with A10 results in:

$$\tilde{h} (\mathbf{r}_\theta^b - \mathbf{r}^M) : \mathbf{n} = h^M (\mathbf{r}_\theta^b - \mathbf{r}^M) : \mathbf{n} + \sqrt{\frac{3}{2}} \frac{1}{L} dm^M \quad (\text{A12})$$

The combination of Equations (6), (16) (A11) and (A12) leads to the final Equation (18).

APPENDIX II – IMPACT ON UNDRAINED CYCLIC RESPONSE

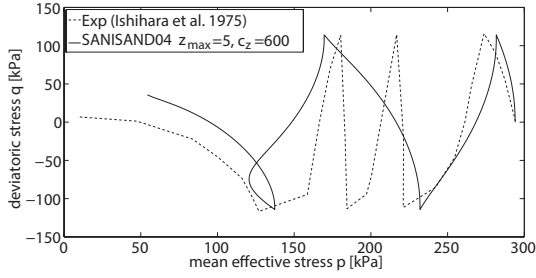
While the main body of the paper focused on the modelling and simulation of drained cyclic strain accumulation, some space is given in this appendix to compare the proposed model and the parent SANISAND04 formulation in terms of undrained cyclic performance. For this purpose, the experimental results from Ishihara *et al.* (1975) are taken as a reference after Dafalias & Manzari (2004) – in particular, an undrained cyclic triaxial test performed on a Toyoura sand specimen at constant cell pressure $p_{in} = 294$ kPa, initial void ratio $e_{in} = 0.808$ and amplitude of applied deviatoric stress $q_{ampl} = 114.2$ kPa. The SANISAND04 parameters shared by the proposed model are reported in Table A1 as identified by Dafalias & Manzari (2004).

The comparison between experimental data and SANISAND04 simulation is reported in Figure A2a. The SANISAND04 model captures the cyclic decrease in effective mean stress, in a way positively affected by the enhanced post-dilation contractancy achieved through the fabric-tensor formulation. However, the model does not accurately predict the pore pressure build-up during each cycle and, in turn, the number of cycles required to reach the phase transformation line (PTL). Conversely, Figure A2b shows the improved performance of the proposed model, based on the memory surface concept combined with the new dilatancy coefficient defined in Equation (21). The proposed model accounts for the gradual stiffening over consecutive cycles and predicts better the number of loading cycles to phase transformation. Comforting predictions are also obtained in terms of pore pressure values beyond phase transformation, along with the nearly nil effective mean stress reached upon unloading. Overall, the new memory-surface-based flow rule seems a promising alternative to the approach followed by Dafalias & Manzari (2004).

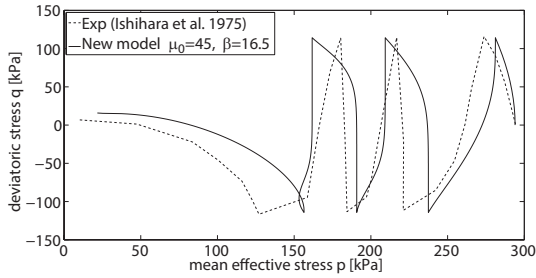
As highlighted in Figure A2c in comparison to Figure A2b, the proposed model offers higher flexibility in reproducing the undrained cyclic behaviour, depending on the set of cyclic parameters μ_0 , ζ and β selected. In general, the initial pore pressure build-up prior to phase transformation can be controlled through the parameter μ_0 ; the post-dilation stress path is mainly governed by the parameter β , which affects indirectly the shrinkage of the memory surface – the larger β , the smaller the minimum effective stress reached upon post-dilation unloading.

Table A1. Toyoura sand parameters shared by SANISAND04 and the new model – after tests by Ishihara *et al.* (1975)

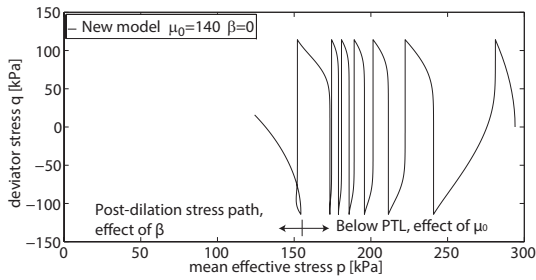
Elasticity		Critical state					Yield surface	Plastic modulus			Dilatancy	
G_0	ν	M	c	λ_c	e_0	ξ	m	h_0	c_h	n^b	A_0	n^d
125	0.05	1.25	0.712	0.019	0.934	0.7	0.01	7.05	0.968	1.1	0.704	3.5



(a) Comparison between experimental result (Ishihara *et al.*, 1975) and SANISAND04 simulation result (Dafalias & Manzari, 2004).



(b) Comparison between experimental result (Ishihara *et al.*, 1975) and new model simulation result ($\mu_0 = 45$, $\zeta = 0.00001$, $\beta = 16.5$).



(c) Influence of μ_0 and β on the undrained performance of the new model ($\mu_0 = 150$, $\zeta = 0.00001$, $\beta = 0$).

Fig. A2. Undrained cyclic behavior of Toyoura sand. Test/simulation settings: $p_{in} = 294$ kPa, $e_{in} = 0.808$, $q^{amp} = 114.2$ kPa.